arXiv:2307.08695v3 [cs.CV] 3 Oct 2024

NVDS⁺: Towards Efficient and Versatile Neural Stabilizer for Video Depth Estimation

Yiran Wang, Min Shi, Jiaqi Li, Chaoyi Hong, Zihao Huang, Juewen Peng, Zhiguo Cao, *Member, IEEE*, Jianming Zhang, Ke Xian, and Guosheng Lin, *Member, IEEE*

Abstract—Video depth estimation aims to infer temporally consistent depth. One approach is to finetune a single-image model on each video with geometry constraints, which proves inefficient and lacks robustness. An alternative is learning to enforce consistency from data, which requires well-designed models and sufficient video depth data. To address both challenges, we introduce NVDS⁺ that stabilizes inconsistent depth estimated by various single-image models in a plug-and-play manner. We also elaborate a large-scale Video Depth in the Wild (VDW) dataset, which contains 14,203 videos with over two million frames, making it the largest natural-scene video depth dataset. Additionally, a bidirectional inference strategy is designed to improve consistency by adaptively fusing forward and backward predictions. We instantiate a model family ranging from small to large scales for different applications. The method is evaluated on VDW dataset and three public benchmarks. To further prove the versatility, we extend NVDS⁺ to video semantic segmentation and several downstream applications like bokeh rendering, novel view synthesis, and 3D reconstruction. Experimental results show that our method achieves significant improvements in consistency, accuracy, and efficiency. Our work serves as a solid baseline and data foundation for learning-based video depth estimation. Code and dataset are available at: https://github.com/RaymondWang987/NVDS

Index Terms—video depth estimation, natural-scene depth dataset, temporal consistency, dense prediction, semantic segmentation

1 Introduction

Monocular video depth estimation serves as a prerequisite for a variety of video applications, such as bokeh rendering [1], [2], 2D-to-3D video conversion [3], and novel view synthesis [4], [5], [6]. An ideal video depth model should exhibit both spatial accuracy and temporal consistency. Although recent developments in single-image depth models [7], [8], [9], [10], [11], [12], [13] and datasets [14], [15], [16], [17] have notably improved the spatial accuracy, how to obtain temporal consistency, i.e., removing flickers in the predicted depth sequences, remains an unresolved question. The prevailing video depth approaches [18], [19], [20] require test-time training. During inference, these methods finetune a single-image depth model on each specific testing video with geometry constraints and pose estimation, which are faced with two primary issues: limited robustness and heavy computation overhead. Due to heavy reliance on camera poses, *e.g.*, CVD [18] shows erroneous predictions and robust-CVD [19] produces artifacts for many videos with inaccurate pose estimation [19], [21]. Moreover, test-time training is a time-consuming process. CVD [18] takes 40 minutes for 244 frames on four NVIDIA Tesla M40 GPUs.

This motivates us to develop a learning-based model that learns to enforce consistency from video depth data. However, akin to all the deep-learning models, learning-based paradigm necessitates proper model design and sufficient training data. In our scenario, where the scale and diversity

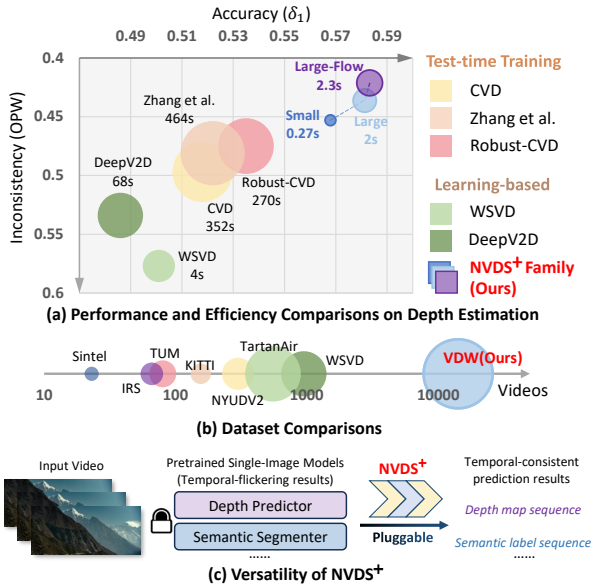


Figure 1: **(a) Performance and efficiency comparisons on depth estimation**. We provide NVDS⁺ model family from $\text{NVDS}^{+}_{\text{Large}}$ for the best performance to $\text{NVDS}^{+}_{\text{Small}}$ for real-time processing. Smaller circles mean faster speed. We also propose the flow-guided consistency fusion strategy (Large-Flow) to further enhance the consistency. NVDS⁺ outperforms prior arts by large margins. **(b) Dataset comparisons**. Larger circles mean larger amounts of frames. We present VDW dataset, the largest video depth dataset in the wild with diverse scenes. **(c) Versatility of NVDS⁺.** We naturally extend the pluggable NVDS⁺ to the video semantic segmentation task to prove the generality of our framework.

This work is supported by the National Natural Science Foundation of China under Grant 62406120. YW, MS, JL, CH, ZH, and ZC are with School of AIA, Huazhong University of Science and Technology (e-mail: {wangyiran,min_shi,lijiaqi_mail,cyhong,zihaohuang,zgcao}@hust.edu.cn).
KX is the corresponding author, with School of AIA and School of EIC, Huazhong University of Science and Technology (e-mail: kxian@hust.edu.cn).
JZ is with Adobe Research (e-mail: jianmzha@adobe.com).
JP and GL are with College of Computing and Data Science, Nanyang Technological University (e-mail: {juewen.peng,gslin}@ntu.edu.sg)

of video depth data are limited, prior learning-based methods [22], [23], [24], [25] exhibit inferior performance compared to test-time-training-based ones. Furthermore, these methods can not benefit from well-trained single-image depth predictors [7], [8], [10], [26]. Both the model design and the availability of data persist as crucial challenges.

To address the two aforementioned challenges, based on our preliminary conference paper NVDS [27], we propose a flexible learning-based framework termed NVDS$^+$, which can be directly applied to different single-image depth models. NVDS$^+$ comprises a depth predictor and a stabilization network. The depth predictor can be any off-the-shelf single-image depth model. Different from previous learning-based methods [22], [23], [24], [25] that function as stand-alone models, NVDS$^+$ is a plug-and-play refiner for different depth predictors. Specifically, the stabilization network processes initial flickering depth estimated by depth predictors and outputs temporally consistent results. Therefore, NVDS$^+$ can benefit from the depth models without extra effort. As for the design of stabilization network, inspired by the attention [28] mechanism in other video tasks [29], [30], [31], [32], we adopt a cross-attention module in our framework. Each frame attends relevant information from adjacent frames for consistency.

Apart from the pluggable stabilization network, we also propose a training-free bidirectional inference strategy to further enlarge temporal receptive field and improve consistency, where outputs are obtained by adaptively fusing the forward and backward predictions. Specifically, we devise a flow-guided consistency fusion strategy to generate the fusion weights. Since frames or pixels with larger motions should have lower relevance with the final target depth, we will give smaller weights to the pixels with large motion amplitudes. Optical flow [33], [34] is adopted to measure motion amplitudes of relevant frames and pixels. Bidirectional depth results are adaptively fused according to motions and relevance maps between reference and target frames. As shown in Fig. 1(a), our model with flow-guided consistency fusion (Large-Flow) achieves even better consistency.

To balance efficiency and performance for different applications, we provide a model family of NVDS$^+$, ranging from small to large scales. To achieve the best performance, we implement our NVDS$^+_{\textbf{Large}}$ working with different top-performing depth predictors [7], [8], [10]. On the other hand, the NVDS$^+_{\textbf{Small}}$ model is built in pursuit of real-time processing, cooperating with varied lightweight depth predictors [8], [26]. As shown in Fig. 1(a), all our implementations outperform previous approaches in terms of consistency, accuracy, and efficiency significantly.

Moreover, we collect a large-scale natural-scene video depth dataset, Video Depth in the Wild (VDW), to support the training of robust learning-based models. Current video depth datasets are mostly closed-domain [35], [36], [37], [38], [39]. A few in-the-wild datasets [40], [41], [42] are still limited in quantity, diversity, and quality, *e.g.*, Sintel [40] only contains 23 animated videos. In contrast, our VDW dataset contains $14{,}203$ stereo videos of over 200 hours and $2.23M$ frames from four different data sources, including movies, animations, documentaries, and web videos. We adopt a rigorous data annotation pipeline to obtain high-quality disparity ground truth for these data. As shown in Fig. 1(b), to the best of our knowledge, VDW is the largest in-the-wild video depth dataset with diverse scenes.

We conduct evaluations on VDW and three public benchmarks: Sintel [40], NYUDV2 [37], and KITTI [35]. Our method achieves state-of-the-art in both accuracy and consistency. We also fit several different depth predictors [7], [8], [10], [26] into our framework, which demonstrates that the NVDS$^+$ can stabilize the flickering results from different depth predictors without any extra effort. Besides, our NVDS$^+_{\textbf{Small}}$ only has 5M parameters and achieves a real-time processing throughput of over 30 fps.

As two exemplar tasks in dense prediction [7], depth estimation and semantic segmentation are both important for downstream applications like autonomous driving and virtual reality. To demonstrate the versatility of NVDS$^+$ for video dense prediction, we extend our framework to video semantic segmentation [32], [43], [44], [45], [46], [47], as shown in Fig. 1(c). Similar to video depth estimation, video semantic segmentation aims to predict both accurate and consistent semantic labels for video frames. Naturally, we can use different single-image semantic segmentation models [48], [49] as semantic segmenters to output initial predictions. Then, through the plug-and-play paradigm, the neural stabilizer can stabilize the flickering results to improve the consistency. Our NVDS$^+$ attains state-of-the-art performance on CityScapes [50] dataset and outperforms stand-alone video semantic segmentation models [44], [46], further demonstrating the generality of the proposed NVDS$^+$ framework. Our main contributions are summarized as follows:

- We propose a plug-and-play and bidirectional learning-based framework NVDS$^+$, which can be directly adapted to different depth predictors to remove flickers.
- We propose VDW dataset, currently the largest video depth dataset in the wild with the most diverse scenes.
- The flow-guided consistency fusion strategy is proposed to further enhance the consistency, which can adaptively fuse the bidirectional results according to motion amplitudes between relevant frames and pixels.
- We implement a comprehensive model family, from NVDS$^+_{\textbf{Large}}$ model for the best performance to the NVDS$^+_{\textbf{Small}}$ model for real-time applications.
- The NVDS$^+$ framework is naturally extended to the video semantic segmentation task and also achieves state-of-the-art performance in both accuracy and consistency.

Note that this paper is an extension of a conference version [27]. Compared with the conference version [27], we upgrade NVDS [27] to NVDS$^+$ with sufficient explorations in the following aspects: i) We provide a model family of NVDS$^+$ for performance-efficiency trade-off; ii) We further explore the bidirectional inference strategy, proposing the flow-guided consistency fusion to adaptively fuse bidirectional results; iii) We prove the versatility of our framework for video dense prediction by extending NVDS$^+$ to video semantic segmentation; iv) More comprehensive evaluations including results on KITTI [35] and CityScapes [50] are conducted to prove our superiority; v) We showcase capabilities of NVDS$^+$ on downstream applications, including bokeh rendering, 3D video conversion, space-time view synthesis, and point cloud reconstruction. Please refer to our project page, demo video, and supplement for more details.

2 Related Work

Consistent Video Depth Estimation. In addition to predicting spatial-accurate depth, the core task of consistent video depth estimation is to achieve temporal consistency, *i.e.*, removing the flickering effects between consecutive frames. Current video depth estimation approaches can be categorized into test-time training ones and learning-based ones. Test-time-training-based methods train an off-the-shelf single-image depth estimation model on testing videos during inference with geometry [18], [19], [20] and pose [19], [21], [51] constraints. The test-time training can be time-consuming. For example, as illustrated by CVD [18], their method takes 40 minutes on 4 NVIDIA Tesla M40 GPUs to process a video of 244 frames. Besides, these approaches are not robust on in-the-wild videos as they heavily rely on camera poses, which are not reliable for natural scenes. In contrast, the learning-based approaches train models on video depth datasets by spatial and temporal supervision. ST-CLSTM [24] adopts long short-term memory (LSTM) to model temporal relations. FMNet [23] restores the depth of masked frames by the unmasked ones with convolutional self-attention [30]. TC-Depth [52] improves consistency by pixel-wise similarities and self-supervision with camera pose. Cao *et al.* [25] adopt a spatial-temporal propagation network trained by knowledge distillation [53], [54]. Khan *et al.* [55] and CODD [56] seek online depth estimation of stereo videos through point-based fusion and temporal depth aggregation respectively. ViTA [57] utilizes a transformer adaptor with temporal embeddings in attention blocks. MAMo [58] proposes the memory update and memory attention mechanism to predict more accurate depth with temporal information. However, those methods cannot refine the results from different single-image depth models for consistency in a plug-and-use style. Their performance on consistency and accuracy is also limited. For example, as shown by FMNet [23], ST-CLSTM [29] only exploits subsequences of several frames and produces flickers in the outputs. In this paper, we propose the NVDS$^+$ framework, which can be directly adapted to off-the-shelf depth models by the pluggable paradigm without extra training.

Video Depth Datasets. According to the scenes of samples, existing video depth datasets can be categorized into closed-domain datasets and natural-scene datasets. Closed-domain datasets only contain samples in certain scenes, *e.g.*, indoor scenes [37], [38], [39], office scenes [36], and autonomous driving [35]. To enhance the diversity of samples, natural-scene datasets are proposed, which use computer-rendered videos [40], [41] or crawl stereoscopic videos from YouTube [42]. However, the scene diversity and scale of these datasets are still very limited for training robust video depth estimation models that can predict consistent depth in the wild. For instance, WSVD [42], which shares a few similar data annotation steps with the proposed VDW dataset, only contains 533 YouTube videos with varied quality and insufficient diversity. Sintel [40] only contains 23 animated videos. To better train and benchmark video depth models, we propose our VDW dataset with $14{,}203$ videos from 4 different data sources. To the best of our knowledge, our VDW dataset is currently the largest video depth dataset in the wild with the most diverse scenes.

Lightweight Depth Models. Some lightweight single-image depth models are proposed for real-time applications. Wang *et al.* [9] leverage a large teacher model to improve the accuracy of the student network by distillation [54], [59]. MiDaS [8] mixes multiple training data in diverse domains to enhance the generality of their MiDaS-Small [8] model. Birkl *et al.* [26] utilize the lightweight backbone SwinV2-Tiny [60] to achieve balanced speed and accuracy. Due to the limited model capacity, these lightweight single-image models also suffer from inaccurate and inconsistent predictions on video data. The key challenge is to stabilize these lightweight models and maintain the high efficiency, which is essential for real-time depth-based video applications. However, the prevailing lightweight video depth model ST-CLSTM [24] is independent and still produces obvious flickers. For real-time consistent video depth estimation, we implement our NVDS$^+_{\textbf{Small}}$, which can stabilize different lightweight depth predictors in a pluggable manner and achieve real-time throughput of over 30 fps. To satisfy different applications, we also provide a comprehensive NVDS$^+$ model family from small to large scales.

Video Semantic Segmentation. Video semantic segmentation and depth estimation are two principal tasks in video dense prediction [7]. These two tasks jointly support applications like virtual reality and autonomous driving. Similar to video depth estimation [18], [19], [20], [23], [24], [57], temporal consistency is of vital importance for video semantic segmentation [32], [43], [44], [46]. Various approaches have been proposed to predict accurate and consistent segmentation maps. ETC [43] utilizes knowledge distillation [53], [54], [59] and optical flow [61] to supervise the consistency of segmentation maps. TMANet [47] adopts self-attention [28] to build inter-frame correlations. MRCFA [44] mines the temporal relations by multi-scale affinities across adjacent frames. CFFM [32] leverages the feature assembling and cross-frame mining modules to build video contextual relations. IFR [45] utilizes the unlabeled frames to reconstruct the features of labeled frames within a video. SSLTM [46] simultaneously uses adjacent and distant frames to construct short- and long-term correlations. However, these prior arts are still stand-alone models, which can not enforce temporal consistency on different single-image semantic segmentation models. To this end, we naturally extend NVDS$^+$ to video semantic segmentation and prove the versatility of our framework. Single-image segmentation models are considered as initial semantic segmenters. NVDS$^+$ can stabilize different semantic segmenters [48], [49] in the effective plug-and-play paradigm.

Blind Video Consistency and Deflickering. Blind video consistency [62], [63], [64] constructs general approaches for extending image processing algorithms to videos with consistency, including colorization, enhancement, style transfer, and intrinsic decomposition. Bonneel *et al.* propose a gradient-domain technique to achieve blindness and generality of different tasks. Lai *et al.* [63] adopt a deep recurrent network [65] for temporal consistency. Lei *et al.* [64] leverage the deep video prior and reweighted training strategy to address the inconsistency. All-In-One-Deflicker [66] further advances the task by removing additional guidance of manual annotations and extra consistent videos. Discussing these methods could be illuminating for video depth estimation.

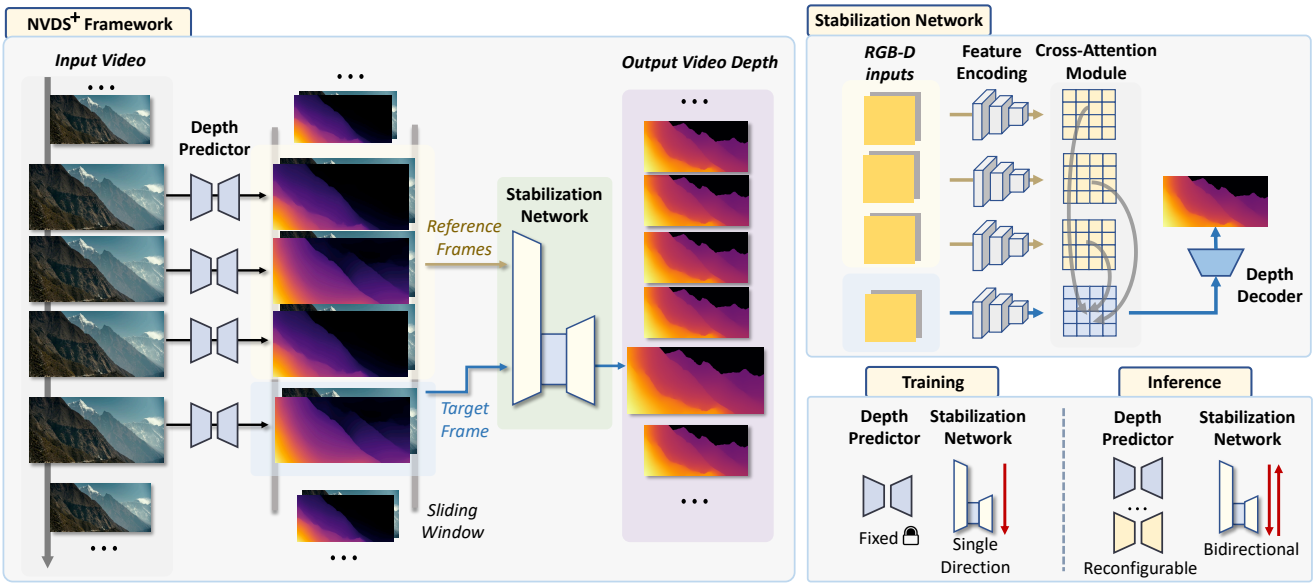


Figure 2: **Overview of the NVDS⁺ framework.** Our framework consists of a depth predictor and a stabilization network. The depth predictor can be any single-image depth model which produces initial flickering depth maps. Then, the stabilization network refines the flickering depth maps into temporally consistent ones. The stabilization network functions with a sliding window. The frame to be predicted fetches information from adjacent frames for stabilization. During inference, our NVDS⁺ framework can be directly adapted to any off-the-shelf depth predictors in a plug-and-play manner. We also devise bidirectional inference with flow-guided consistency fusion to further improve the consistency.

3 NVDS⁺ Framework

As shown in Fig. 2, the NVDS⁺ framework consists of a depth predictor and a stabilization network. The depth predictor predicts the initial flickering depth for each frame. The stabilization network converts the depth maps into temporally consistent ones. Our NVDS⁺ framework can coordinate with any off-the-shelf single-image depth models as depth predictors. We also devise a bidirectional inference strategy with flow-guided consistency fusion to further enlarge the temporal receptive field and enhance consistency.

3.1 Stabilization Network

The stabilization network takes RGB frames along with initial depth maps as inputs. A backbone [48] encodes the input sequences into depth-aware features. The next step is to build inter-frame correlations. We use a cross-attention module to refine the depth-aware features with temporal information from relevant frames. Finally, the refined features are fed into a decoder which restores depth maps with temporal consistency.

Depth-aware Feature Encoding. Our stabilization network works with a sliding window: each frame refers to a few previous frames, serving as reference frames, to stabilize the depth. We denote the frame to be predicted as the target frame. Each sliding window consists of four frames.

Due to the varied scale and shift of different depth predictors, the initial depth maps within a sliding window $\mathbf{F} = \{F_1, F_2, F_3, F_4\}$ should be normalized into F_i^{norm}:

$$F_i^{norm} = \frac{F_i - \min(\mathbf{F})}{\max(\mathbf{F}) - \min(\mathbf{F})}, i \in \{1, 2, 3, 4\}. \quad (1)$$

Then, the normalized depth maps are concatenated with the RGB frames to form a RGB-D sequence. We use a transformer backbone [48] to encode the RGB-D sequence into depth-aware feature maps.

Cross-attention Module. With the depth-aware features, the subsequent phase entails the establishment of inter-frame correlations. We leverage a cross-attention module to build temporal and spatial dependencies across pertinent video frames. Specifically, in the cross-attention module, the target frame selectively attends the relevant features in the reference frames to facilitate depth stabilization. Pixels in the target frame feature maps serve as the query in the cross-attention operation [28], while the keys and values are generated from the reference frames.

Computational cost can become prohibitively high when employing cross-attention for each position in depth-aware features. Hence, we utilize a patch merging strategy [67] to down-sample the target feature map. Besides, we also restrict the cross-attention into a local window, whereby each token in the target features can only attend a local window in the reference frames. Let T denote the depth-aware feature of the target frame, while R_1, R_2 and R_3 represent the features for the three reference frames. T is partitioned into 7×7 patches with no overlaps; each patch is merged into one token $\mathbf{t} \in \mathbb{R}^c$, where c is the dimension. For each $\mathbf{t}$, we conduct a local window pooling on R_1, R_2, and R_3 and stack the pooling results into $R_p \in \mathbb{R}^{c \times 3}$. Then, the cross-attention is computed as:

$$\mathbf{t}' = \text{softmax}\frac{W_q\mathbf{t}\,(W_k R_p)^T}{\sqrt{c}} W_v R_p\,, \quad (2)$$

where W_q, W_k, and W_v are learnable linear projections. The cross-attention layer is incorporated into a standard transformer block [28] with residual connection and multi-layer perceptron (MLP). We denote the resulting target feature map refined by the cross-attention module as T_{tem}.

Ultimately, a depth decoder with feature fusion modules [68], [69] integrates the depth-aware feature of the target frame (T) with the cross-attention refined feature T_{tem}, and predicts the consistent depth map for target frame.

3.2 Training the Stabilization Network

In the training phase, only the stabilization network is optimized. The depth predictor is the freezed pre-trained DPT-Large [7]. For the stabilization network, we apply spatial and temporal loss that supervises the depth accuracy and temporal consistency respectively. The training loss can be formulated by:

$$\mathcal{L} = \sum_{n=2}^{N} \left[\mathcal{L}_s(n-1) + \mathcal{L}_s(n) + \lambda \mathcal{L}_t(n, n-1) \right] , \quad (3)$$

where $\mathcal{L}_s(n-1)$ and $\mathcal{L}_s(n)$ denote the spatial loss of frame $n-1$ and n. N represents the video frame number. $\mathcal{L}_t(n, n-1)$ denotes the temporal loss between frame $n-1$ and n.

We adopt the widely-used affinity invariant loss and gradient matching loss [7], [8], [14] as the spatial loss $\mathcal{L}_s$. As for the temporal loss, we adopt the optical flow based warping loss [23], [25] to supervise temporal consistency:

$$\mathcal{L}_t(n, n-1) = \frac{1}{M} \sum_{j=1}^{M} O^{(j)}_{n \Rightarrow n-1} |D^{(j)}_n - \hat{D}^{(j)}_{n-1}| , \quad (4)$$

where $|\cdot|$ represents the absolute value function. $\hat{D}_{n-1}$ is the predicted depth D_{n-1} warped by the optical flow $FL_{n \Rightarrow n-1}$. In our implementation, we adopt GMFlow [33] for optical flow. $O_{n \Rightarrow n-1}$ is the mask calculated as [23], [25]. M denotes pixel numbers. See supplement for more details on loss functions.

3.3 Bidirectional Inference

Expanding the temporal receptive range can be beneficial for consistency, *e.g.*, adding more former or latter reference frames. However, directly training the stabilization network with bidirectional reference frames will introduce large training burdens. To remedy this, we only train the stabilization network with the former three reference frames. To further enlarge the temporal receptive field and enhance consistency, we introduce a bidirectional inference strategy.

Unlike the training phase, during inference, both the former and latter frames will be used as the reference frames. An additional sliding window is added, where the reference frames are the subsequent three frames of the target. Let us define the stabilizing process as a function $\mathcal{S}(V_t, \mathbf{V}_r)$, where V_t and $\mathbf{V}_r$ denotes the target RGB-D frame and the reference frames set. The stabilizing function $\mathcal{S}$ does not involve warping-based alignment, as it could lead to incorrect edges and artifacts. When denoting the RGB-D sequence as $\{V_j | \, j \in 1, 2, \cdots, N\}$, N represents the frame number of a certain video, using this additional sliding window for stabilization can be formulated as:

$$D^{post}_n = \mathcal{S}(V_n, \{V_{n+1}, V_{n+2}, V_{n+3}\}) , \quad (5)$$

where V_n denotes the target frame. Likewise, using the original sliding window for stabilization can be denoted by:

$$D^{pre}_n = \mathcal{S}(V_n, \{V_{n-1}, V_{n-2}, V_{n-3}\}) . \quad (6)$$

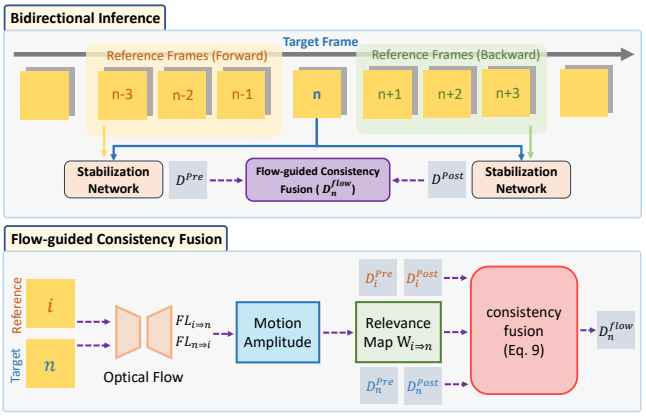


Figure 3: **Bidirectional inference strategy with flow-guided consistency fusion**. Frames or pixels displaying significant motions are considered less relevant to the final target depth. We adaptively fuse the bidirectional depth outcomes of the reference and target frames according to the motion amplitudes and relevance maps derived from optical flow [33], [61]. This technique can further extend the temporal receptive range and improve the consistency.

We ensemble the bidirectional results for a larger temporal receptive field as:

$$D^{bi}_n = \frac{(D^{pre}_n + D^{post}_n)}{2} . \quad (7)$$

D^{bi}_n denotes the depth prediction of the nth frame (target frame). The bidirectional inference can further improve the temporal consistency as demonstrated in Table 5.

Note that, the cross-attention module is shared by the two sliding windows for inference. Besides, the initial depth maps and depth-aware features are pre-computed. Hence, the bidirectional inference only increases the inference time by 30% compared with single-direction inference and brings no extra computation for the training process.

The assumption of bidirectional inference is the availability of a few future reference frames, which is primarily applicable to existing videos or streaming videos with some subsequent frames. The strategy brings additional latency, which is not desirable in online applications. Thus, it is deemed optional to further enhance consistency during test time, since our stabilization network can already produce highly consistent results only with forward predictions. To improve our applicability in real-time applications, we develop the lightweight NVDS$^{\star}_{\textbf{Small}}$ model with end-to-end real-time throughput of over 30 fps.

3.4 Flow-Guided Consistency Fusion

The bidirectional inference strategy can enhance the temporal consistency based on the forward and backward predictions. The direct averaging as Eq. 7 is actually a straightforward yet effective way to merge D^{pre}_n and D^{post}_n using fixed weights, which expands the temporal receptive range without introducing heavy computational costs. However, compared with the direct averaging, using adaptive weights to fuse the bidirectional outcomes of reference and target frames can be more reasonable, since frames or pixels that



Figure 4: **Visualizations of flow-guided fusion.** We visualize the intermediate results of flow-guided consistency fusion. For the relevance maps W_i, brighter colors indicate higher values, while darker colors indicate lower fusion weights.

exhibit larger motions relative to the target frame should be deemed less relevant for the final target depth.

To this end, we advance the bidirectional inference with a flow-guided consistency fusion strategy, which enables the adaptive fusion of bidirectional depth results from reference and target frames. As shown in Fig. 3, we utilize optical flow [33], [61] to assess the pixel-wise motion amplitudes and relevance maps between reference and target frames. The bidirectional optical flow $FL_{i\Rightarrow n}$ and $FL_{n\Rightarrow i}$ are computed between the reference frame $i \in \{n \pm 3, n \pm 2, n \pm 1\}$ and the target frame n. Motion amplitude between reference and target frames can be estimated by the magnitude (*i.e.*, Frobenius norm) of optical flow [33], [61]. Pixels with larger motions in the reference frames tend to have lower relevance to the corresponding pixels in the target frame. To quantify this, we calculate the pixel-wise adaptive relevance map W_i as follows:

$$W_i = \exp\left[-\alpha \cdot (||FL_{i\Rightarrow n}||_F + ||FL_{n\Rightarrow i}||_F)\right], \quad (8)$$

where the coefficient α serves to restrict the weights assigned to pixels exhibiting significant motions. A larger value of α results in reduced weights for those pixels with more pronounced motions in the reference frames.

The final depth results of target frame n with flow-guided consistency fusion can be articulated by:

$$D_n^{flow} = \beta \cdot D_n^{bi} + (1-\beta) \cdot \sum_i (W_i \cdot (D_i^{pre} + D_i^{post})), \quad (9)$$

in which β and $1-\beta$ represent the weights of the bidirectional averaging as Eq. 7 and the enhanced flow-guided consistency fusion, respectively. The second term of flow-guided consistency fusion solely incorporates information from the reference frames. Thus, we integrate the above two terms and further achieve an improvement in the temporal consistency beyond that of simple averaging, as demonstrated in Table 5.

For better understanding, we visualize some intermediate results in Fig. 4. For the first sample, a deer runs quickly across the scene. The relevance map accurately identifies the positions of the moving deer in both frames (*e.g.*, the overlapping antlers) and produces low fusion weights in the moving areas. For the second sample, walking people are also assigned low relevance values. These regions exhibit significant motion, leading to pixel misalignment and low depth relevance. Thus, our strategy tends not to fuse the unreliable depth of reference frames, but preserves the original bidirectional depth D_n^{bi} of the target frame. In this way, our method can improve the consistency without introducing errors in the presence of motion.

3.5 NVDS⁺ Real-time Model and Model Family

The application paradigms of our NVDS⁺ can be categorized into two distinct aspects. On the one hand, in pursuit of the best performance on both the spatial accuracy and temporal consistency, $\text{NVDS}^{+}_{\textbf{Large}}$ utilizes various top-performing depth models [7], [8], [10] as the single-image depth predictors during inference. On the other hand, for real-time processing and applications, $\text{NVDS}^{+}_{\textbf{Small}}$ employs different lightweight depth predictors [8], [26].

To develop the $\text{NVDS}^{+}_{\textbf{Small}}$ model, we use a lightweight attention-based backbone [48] to encode the depth-aware features. Compared with $\text{NVDS}^{+}_{\textbf{Large}}$, the attention layers and the token embedding dimensions of $\text{NVDS}^{+}_{\textbf{Small}}$ are reduced. Additionally, we have implemented model pruning [70] on $\text{NVDS}^{+}_{\textbf{Small}}$ to further boost its efficiency. As detailed in Sec. 5.4, $\text{NVDS}^{+}_{\textbf{Small}}$ achieves a real-time processing speed of over 30 fps, enforcing temporal consistency and significantly surpassing previous lightweight depth models [8], [24], [26] in performance. Please refer to Sec. 3.7 for more implementation details of the large and small models.

3.6 Extension to Video Semantic Segmentation

Analogous to video depth estimation [18], [19], [23], the temporal consistency is equally crucial for video semantic segmentation [32], [43], [44], [45], [46], [47]. It is a logical progression for us to extend our NVDS⁺ framework to the video semantic segmentation task.

We firstly delineate the inputs and outputs. With RGB frames as inputs, video semantic segmentation models [32], [43], [44], [45], [46], [47] are trained to predict the per-pixel probability $\mathcal{P}$ with C channels for each frame, in which C refers to the number of semantic classes. The one-channel semantic label predictions $\mathcal{Q}$ are then derived by performing an $Argmax$ operation on the channel dimension of $\mathcal{P}$.

In our case, we employ various pre-existing single-image semantic segmentation models [48], [49] as the initial semantic segmenter. Our objective is to enhance the temporal consistency from the initial flickering results in a plug-and-play manner. Within a sliding window, the RGB frames are concatenated with the one-channel label predictions $\mathcal{Q}$ from semantic segmenters, serving as the input for our stabilization network. We omit the normalization operation in Eq. 1, as the label predictions $\mathcal{Q}$ from different segmenters share a uniform data range and format. The output of our stabilization network is adjusted to C channels as

the probability predictions. We apply a common semantic decoder [32], [48] for output and the cross entropy (CE) loss for supervision. Moreover, the bidirectional inference and the flow-guided consistency fusion are conducted on the probability predictions, considering that merging multiple integral semantic labels would be unsuitable.

Instead of the more fine-grained label probability distributions $\mathcal{P}$, NVDS$^+$ works with the one-channel label predictions $\mathcal{Q}$ for two main reasons. Firstly, the channel number C of $\mathcal{P}$ equals the number of semantic classes, which can be large in practice [50], [71]. Using $\mathcal{P}$ as the multi-frame input significantly increases computational costs during training and inference. Besides, the channel number C differs across datasets and scenarios. The varying input channels could restrict the uniformity and applicability from the perspective of model design. Therefore, NVDS$^+$ stabilizes the one-channel $\mathcal{Q}$ predicted by initial segmenters [48], [49].

With similar settings of the sliding windows, the cross-attention module, and the inference protocol as in video depth estimation, our NVDS$^+$ can effectively stabilize different semantic segmenter [48], [49] in the pluggable paradigm. We attain state-of-the-art performance for video semantic segmentation on CityScapes dataset [50]. With minor modifications, the efficacy of our NVDS$^+$ in both the depth estimation and semantic segmentation underscores the adaptability and versatility of our framework.

3.7 Implementation Details

Depth and Disparity. For all our implementations of video depth, the inputs and outputs of NVDS$^+$ are disparity maps, *i.e.*, the inverse of depth. The models are also supervised by the disparity ground truth from the VDW dataset. We illustrate the reasons for using disparity in the supplement.

Model Architecture. The disparity maps from DPT-Large [7] are used as the input of large and small models during training. For each target frame, we use three reference frames with inter-frame intervals $l = 1$. **NVDS$^+_{\text{Large}}$** adopts DPT-Large [7], MiDaS-v2.1-Large [8], and NeWCRFs [10] as depth predictors during inference. MiDaS-v2.1-Large [8] is the same depth model as test-time-training-based methods [18], [19], [20] for fair comparisons. Mit-b5 [48] is adopted as the backbone to encode depth-aware features. The token embedding dimension c of NVDS$^+_{\text{Large}}$ is 256. **NVDS$^+_{\text{Small}}$** adopts lightweight depth predictors DPT-Swin2-Tiny [26] and MiDaS-v2.1-Small [8]. It utilizes Mit-b0 [48] as the backbone and the token embedding dimension $c = 128$. The small model only adopts the forward prediction for online and real-time applications.

Training Recipe. All frames are resized so that the shorter side equals 384, and then randomly cropped to 384×384 for training. In each epoch, we randomly sample $72{,}000$ input sequences. Note that the sampled frames in each epoch do not overlap. We use Adam optimizer to train the model for 30 epochs with a batchsize of 9. The initial learning rate is 6×10^{-5} and decreases by 1×10^{-5} for every five epochs. When finetuning our model on NYUDV2 [37] and KITTI [35] datasets, we use a learning rate of 1×10^{-5} for only one epoch. In all experiments, the temporal loss weight λ in Eq. 3 is set to 0.2. The coefficient α in Eq. 8 is 10. The weight β of flow-guided consistency fusion in Eq. 9 is 0.5.

Table 1: **Comparisons of video depth datasets.** The 3D Movies dataset of MiDaS [8] is not released and only contains 75k images but not videos. TartanAir [41] only has some limited dynamic scenes (*e.g.*, fish in the ocean sequence). Most videos in TartanAir [41] lack major dynamic objects (*e.g.*, pedestrians). For example, models trained on TartanAir cannot predict satisfactory results in scenes with moving people as such scenes are rare. Our VDW dataset shows advantages in diversity and quantity.

Type	Dataset	Videos	Frames(k)	Indoor	Outdoor	Dynamic	Resolution
Closed Domains	NYUDV2 [37]	464	407	✔	✘	✘	640×480
	KITTI [35]	156	94	✘	✔	✔	1224×370
	TUM [36]	80	128	✔	✘	✔	640×480
	IRS [39]	76	103	✔	✘	✘	960×540
	ScanNet [38]	1,513	2,500	✔	✘	✘	640×480
CG Rendered	Sintel [40]	23	1	✔	✔	✔	1024×436
	TartanAir [41]	1,037	1,000	✔	✔	✘	640×480
Natural Scenes	MiDaS [8]	✘	75	✔	✔	✔	1880×800
	WSVD [42]	553	1,500	✔	✔	✔	$\sim 720p$
	Ours	14,203	2,237	✔	✔	✔	1880×800

Video Semantic Segmentation. The backbone and model parameters significantly influence the performance of semantic segmentation. Thus, we follow the experimental settings of the previous state-of-the-art video semantic segmentation method SSLTM [46] for fair comparisons with similar amounts of parameters. Identical to SSLTM [46], we implement our model and compare different methods using ResNet-50 [72] as the backbone. For the training of our model, only the SegFormer-B1 [48] is used as the initial semantic segmenter. During inference, different single-image semantic segmenters are used for the plug-and-play paradigm, including SegFormer-B1, SegFormer-B3 [48], and OneFormer [49]. Other settings such as reference frames and inter-frame intervals are the same as video depth.

The ResNet-50 [72] backbone is initialized with ImageNet-pretrained [73] weight. Other parts are initialized randomly. We follow the standard training recipe as prior arts [32], [43], [44], [46] on CityScapes dataset [50]. Specifically, frames are cropped to 512×1024 for training and resized to the same resolution during inference. We adopt the commonly-applied single-scale test [32], [44], [46] for simplicity. The Adam optimizer is used to train the model for 30 epochs with a batchsize of 4. The learning rate, the temporal loss weight λ in Eq. 3, the coefficient α in Eq. 8, and the weight β of bidirectional inference in Eq. 9 are all identical to video depth estimation.

4 VDW Dataset

As mentioned in Sec. 1, current video depth datasets are limited in both diversity and volume. To compensate for the data shortage and boost the performance of learning-based video depth models, we elaborate a large-scale natural-scene dataset, Video Depth in the Wild (VDW). To our best knowledge, our VDW dataset is currently the largest video depth dataset with the most diverse video scenes.

Dataset Construction. We collect stereo videos from four data sources: movies, animations, documentaries, and web videos. A total of 60 movies, animations, and documentaries in Blu-ray format are collected. We also crawl 739 web stereo videos from YouTube with the keywords such as "stereoscopic" and "stereo". To balance the realism and



Figure 5: **Examples of our VDW dataset.** Four rows are from web videos, documentaries, animations, and movies, respectively. Sky regions and invalid pixels are masked out.



Figure 6: **Objects presented in our VDW dataset.** We conduct semantic segmentation with Mask2Former [75] trained on ADE20K [71]. Refer to our supplementary document for more detailed construction process and data statistics.

diversity, only 24 movies, animations, and documentaries are retained. For instance, "Seven Wonders of the Solar System" is removed as it contains many virtual scenes. The disparity ground truth is generated with two main steps: sky segmentation and optical flow estimation. A model ensemble method is adopted to remove errors and noises in the sky masks, which can improve the quality of the ground truth and the performance of the trained models, especially on sky regions as shown in Fig. 7. A state-of-the-art optical flow model GMFlow [33] is used to generate the disparity ground truth. Finally, a rigorous data cleaning procedure is conducted to filter the videos that are not qualified for our dataset. Fig. 5 shows some examples of our VDW dataset.

Dataset Statistics. VDW dataset contains 14,203 videos with a total of 2,237,320 frames. The total data collection and processing time takes over six months and about 4,000 man-hours. To verify the diversity of scenes and entities in our dataset, we conduct semantic segmentation by Mask2Former [75] trained on ADE20K [71]. All the 150 categories are covered in our dataset, and each category can be found in at least 50 videos. Fig. 6 shows the word cloud of the 150 categories. We randomly choose 90 videos with 12,622 frames as the test set. The testing videos adopt different data sources from the training data, *i.e.*, different movies, web videos, or animations. VDW not only alleviates the data shortage for learning-based approaches, but also serves as a comprehensive benchmark for video depth.

Comparisons with Other Datasets. As shown in Table 1, the proposed VDW dataset has significantly larger numbers of video scenes. Compared with the closed-domain datasets [35], [36], [37], [38], [39], the videos of VDW are not restricted to a certain scene, which is more helpful to train a robust video depth model. For the natural-scene datasets, our dataset has more than ten times the number of videos as the previous largest dataset WSVD [42]. Although WSVD [42] has $1.5M$ frames, the scenes (video numbers) are limited. MiDaS [8] also proposes their 3D Movies dataset with in-the-wild images and disparity. Compared with the 3D Movies dataset of MiDaS [8], VDW differs in two main aspects: (1) accessibility; and (2) dataset scale and format. MiDaS [8] does not provide related metadata (*e.g.*, timestamps) and data generation scripts. In contrast, we have released the comprehensive VDW Dataset Toolkit [76] and our metadata, allowing researchers to reproduce VDW or generate new datasets. Besides, their 3D Movies dataset [8] only contains $75k$ images, while VDW contains 14,203 videos with $2.237M$ frames. It is also worth noticing that our VDW dataset has higher resolution and a rigorous data annotation and cleaning pipeline. We only collect videos over $1080p$ and crop all our videos to 1880×800 to remove black bars and subtitles. See supplement for more statistics and details.

5 Experiments

To validate the effectiveness and generality of our NVDS$^+$ framework, we carry out experiments on the tasks of video depth estimation and video semantic segmentation, which are two key tasks in dense prediction [7]. For video depth estimation, we evaluate NVDS$^+$ on four different datasets, which contain videos for real-world and synthetic, static and dynamic, indoor and outdoor. We also demonstrate that our flow-guided consistency fusion can further enhance the temporal consistency by adaptively merging the bidirectional disparity results. In order to prove our efficacy in real-time applications, we compare our NVDS$^+_{\text{Small}}$ model with other lightweight single-image depth predictors or video depth models in terms of performance and efficiency. For video semantic segmentation, we conduct evaluations on CityScapes [50] dataset following prior arts [32], [44], [46]. NVDS$^+$ achieves state-of-the-art performance for both tasks, which proves the versatility of our framework.

5.1 Datasets and Evaluation Protocol

In this section, we illustrate the datasets and evaluation protocols for video depth estimation. Please refer to Sec. 5.5 for the experimental details of video semantic segmentation.

VDW Dataset. We use the proposed VDW as the training data for its diversity and quantity on natural scenes. We also evaluate the previous video depth approaches on the test split of VDW, serving as a new video depth benchmark.

Sintel Dataset. Following [19], [20], we use the final version of Sintel [40] to demonstrate the generalization ability of our NVDS$^+$. We conduct zero-shot evaluations on Sintel [40]. All learning-based methods are not finetuned on Sintel dataset.

DAVIS Dataset. DAVIS [77] is a natural-scene dataset for video object segmentation. we also test our NVDS$^+$ on the challenging videos from DAVIS [77] for qualitative comparisons. Please refer to our demo video for video results.

NYUDV2 Dataset. Except for natural scenes, a closed-domain NYUDV2 [37] is adopted for evaluation. It contains 464 videos of indoor scenes. We pretrain the stabilization

Table 2: **Comparisons with the state-of-the-art approaches.** We test the total time of processing eight 640×480 frames on one NVIDIA RTX A6000 GPU. For our NVDS$^+$, we report the performance of our large model with complete designs, *i.e.*, NVDS$^+_{\textbf{Large}}$ with flow-guided consistency fusion. The best performance is in boldface. Second best is underlined.

Type	Method	Time(s)	VDW			Sintel			NYUDV2			KITTI		
			$\delta_1 \uparrow$	$Rel \downarrow$	$OPW \downarrow$	$\delta_1 \uparrow$	$Rel \downarrow$	$OPW \downarrow$	$\delta_1 \uparrow$	$Rel \downarrow$	$OPW \downarrow$	$\delta_1 \uparrow$	$Rel \downarrow$	$OPW \downarrow$
Single Image	MiDaS-v2.1-Large [8]	0.76	0.651	0.288	0.676	0.485	0.410	0.843	0.910	0.095	0.862	0.940	0.088	0.602
	DPT-Large [7]	0.97	<u>0.730</u>	<u>0.215</u>	0.470	**0.597**	<u>0.339</u>	0.612	0.928	0.084	0.811	0.964	0.069	0.585
Test-time Training	CVD [18]	352.58	–	–	–	0.518	0.406	0.497	–	–	–	0.878	0.114	0.374
	Robust-CVD [19]	270.28	0.676	0.261	0.279	0.521	0.422	0.475	0.886	0.103	0.394	0.901	0.097	0.338
	Zhang *et al.* [20]	464.83	–	–	–	0.522	0.342	0.481	–	–	–	–	–	–
Learning Based	ST-CLSTM [24]	0.58	0.477	0.521	0.448	0.351	0.517	0.585	0.833	0.131	0.645	0.890	0.101	0.413
	Cao *et al.* [25]	–	–	–	–	–	–	–	0.835	0.131	–	0.872	0.109	–
	FMNet [23]	3.87	0.472	0.514	0.402	0.357	0.513	0.521	0.832	0.134	0.387	0.886	0.099	0.375
	DeepV2D [22]	68.71	0.546	0.528	0.427	0.486	0.526	0.534	0.924	0.082	0.402	0.972	0.051	0.428
	WSVD [42]	4.25	0.637	0.314	0.462	0.501	0.439	0.577	0.768	0.164	0.683	0.812	0.156	0.497
	Li *et al.* [74]	–	–	–	–	0.475	0.389	–	–	–	–	–	–	–
	ViTA [57]	1.38	0.689	0.243	0.252	0.554	0.376	0.492	0.922	0.092	0.385	0.912	0.095	0.316
	MAMo [58]	–	–	–	–	–	–	–	0.919	0.094	–	<u>0.977</u>	0.049	–
	Ours-Large(MiDaS-v2.1-Large)	1.92	0.701	0.239	<u>0.148</u>	0.532	0.372	<u>0.447</u>	<u>0.941</u>	<u>0.076</u>	<u>0.347</u>	0.970	<u>0.049</u>	<u>0.258</u>
	Ours-Large(DPT-Large)	2.31	**0.742**	**0.208**	**0.129**	<u>0.591</u>	**0.335**	**0.403**	**0.950**	**0.072**	**0.339**	**0.982**	**0.046**	**0.233**

network on VDW and finetune the model on NYUDV2 [37]. We follow the same train/test split as Eigen *et al.* [23], [24], [25], [78] with 249 videos for training and 654 samples from the rest 215 videos for testing.

KITTI Dataset. Similar to NYUDV2 [37] dataset, we also conduct the pretraining and finetuning protocol on KITTI [35], which is another major closed-domain video depth dataset. KITTI [35] is captured by cameras and depth sensors mounted on a driving car and consists of 61 outdoor video scenes. We follow the train/test split as Eigen *et al.* [23], [24], [25], [78] with 32 videos for training and 697 samples from the rest 29 videos for testing.

Evaluation Metrics. We evaluate both the depth accuracy and temporal consistency. For the temporal consistency metric, we adopt the optical flow based warping metric (OPW) following FMNet [23], which can be computed as:

$$OPW = \frac{1}{N-1} \sum_{n=2}^{N} \mathcal{L}_t(n, n-1)\,. \tag{10}$$

We report the average OPW of all the videos in the test sets. As for the depth metrics, we adopt the commonly-applied Rel and $\delta_i (i = 1, 2, 3)$.

5.2 Comparisons with Other Video Depth Methods

Comparisons with the test-time training methods. First focus on the test-time training approaches [18], [19], [20]. As shown in Table 2, our learning-based framework outperforms these approaches by large margins in terms of inference speed, accuracy and consistency. Our NVDS$^+$ shows at least 6.6% and 7.6% improvements for δ_1 and OPW than Robust-CVD [19] on VDW, Sintel [40], NYUDV2 [37], and KITTI [35]. Our learning-based approach is over one hundred times faster than Robust-CVD [19]. Our strong performance demonstrates that learning-based frameworks are capable of attaining great performance with much higher efficiency than test-time-training-based ones [18], [19], [20].

It is also worth-noticing that test-time-training-based approaches are not robust for natural scenes. CVD [18] and Zhang *et al.* [20] fail on some videos on VDW and Sintel [40] due to erroneous pose estimation results. Hence, some of their results are not reported in Table 2. Refer to the supplement for more details. Although Robust-CVD [19] can produce results for all testing videos by jointly optimizing the camera poses and depth, it is still not robust for many videos and produces obvious artifacts as shown in Fig. 7.

Comparisons with the learning-based methods. The proposed NVDS$^+$ also attains better accuracy and consistency than previous learning-based approaches [22], [23], [24], [25], [42], [74] on all the four datasets, including natural scenes and closed domain. As shown in Table 2, on our VDW and Sintel with natural scenes, the proposed NVDS$^+$ shows obvious advantages: improving δ_1 and OPW by over 9% and 18.6% compared with previous learning-based methods. Note that, our NVDS$^+$ can benefit from stronger single-image models and obtain better performance, which will be discussed and proved in Table 10.

To better compare NVDS$^+$ with previous learning-based methods, we only use NYUDV2 [37] or KITTI [35] as training and evaluation data for comparisons. As shown in Table 3, the NVDS$^+$ improves the FMNet [23] by 9.9% and 3.8% in terms of δ_1 and OPW on NYUDV2 [37]. We also achieve better performance than DeepV2D [22], which is the previous state-of-the-art structure-from-motion-based method [21], [22], [79], [80] but can only deal with completely static scenes. The results demonstrate that using our architecture alone can also obtain better performance.

Qualitative Comparisons. We show some qualitative comparisons on natural-scene videos in Fig. 7. We draw the scanline slice over time. Fewer zigzagging pattern means better consistency. The initial estimation of DPT [7] in the seventh row contains flickers and blurs, which are eliminated with the proposed NVDS$^+$, as shown in the last row. Although the test-time-training-based Robust-CVD [19] shows competitive performances on the indoor NYUDV2 [37] dataset, it is not robust on the natural scenes. As can be observed in the fourth row, Robust-CVD produces obvious artifacts due to the erroneous pose estimation.

Besides, we also showcase some visual comparisons on the in-the-wild videos from the DAVIS [77] dataset. As shown in Fig. 8, we present some challenging videos with large camera and object motions (*e.g.*, the motorcycle stunt flying over the hill and the drifting racing car). NVDS$^+$

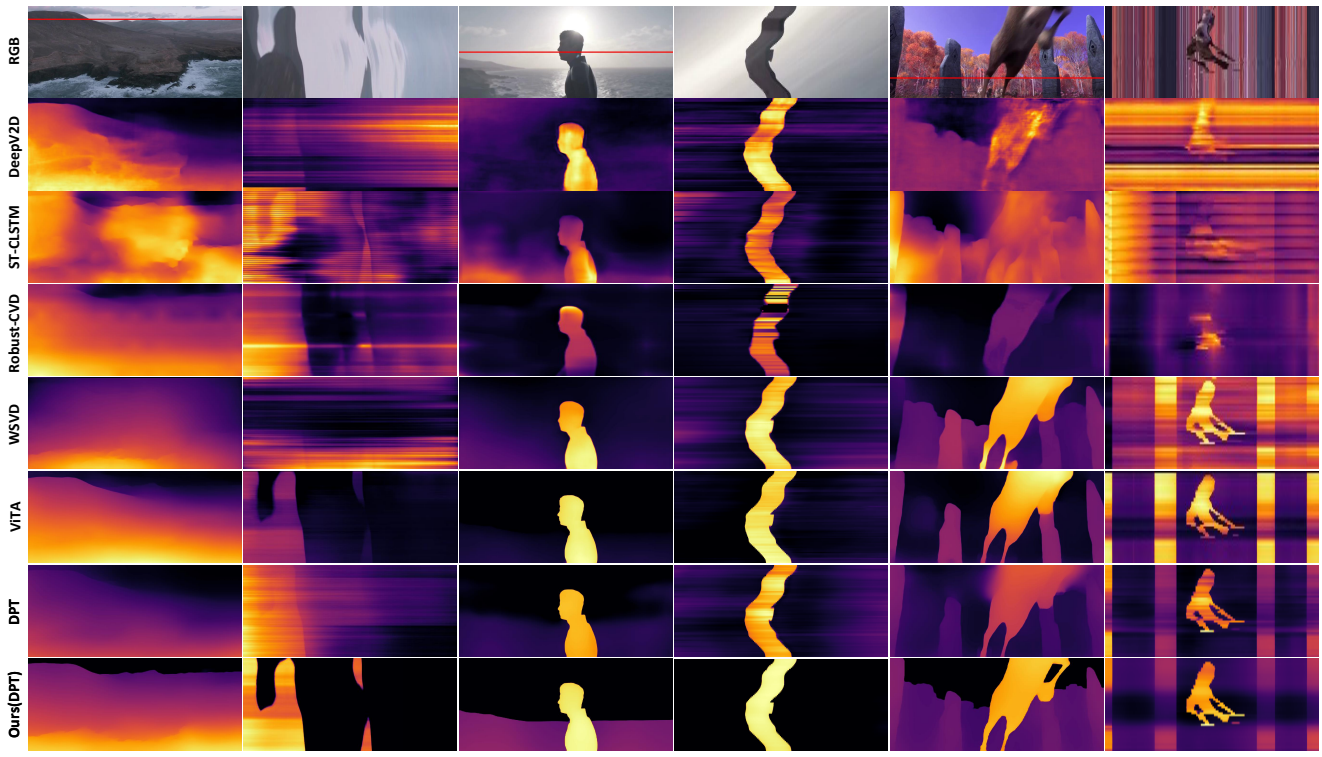


Figure 7: **Qualitative comparisons.** DeepV2D [22] and Robust-CVD [19] show obvious artifacts in those videos. We draw the scanline slice over time; fewer zigzagging pattern means better consistency. Compared with the other video depth methods, our NVDS$^+$ is more robust on natural scenes and achieves better spatial accuracy and temporal consistency.

Table 3: **Comparisons of learning-based approaches on NYUDV2 [37] and KITTI [35]**. All the compared methods use NYUDV2 [37] or KITTI [35] as the training and evaluation data, following the train/test split as Eigen *et al.* [78]. Our NVDS$^+$ trained from scratch also achieves better performance than all the other methods.

Method	$\delta_1 \uparrow$	$\delta_2 \uparrow$	$\delta_3 \uparrow$	$Rel \downarrow$	$OPW \downarrow$
NYUDV2					
SC-DepthV1 [81]	0.813	0.952	0.987	0.143	0.465
SC-DepthV2 [82]	0.820	0.956	0.989	0.138	0.474
SC-DepthV3 [83]	0.848	0.963	0.991	0.123	0.441
ST-CLSTM [24]	0.833	0.965	0.991	0.131	0.645
Cao *et al.* [25]	0.835	0.965	0.990	0.131	–
FMNet [23]	0.832	0.968	0.992	0.134	0.387
DeepV2D [22]	0.924	0.982	0.994	0.082	0.402
Ours-Large-scratch(DPT-Large)	**0.931**	**0.989**	**0.996**	**0.081**	**0.345**
KITTI					
SC-DepthV1 [81]	0.860	0.956	0.981	0.118	0.402
SC-DepthV2 [82]	0.866	0.958	0.981	0.118	0.389
SC-DepthV3 [83]	0.864	0.960	0.984	0.118	0.397
ST-CLSTM [24]	0.890	0.970	0.989	0.101	0.413
Cao *et al.* [25]	0.872	0.962	0.986	0.109	–
FMNet [23]	0.886	0.968	0.989	0.099	0.375
TC-Depth [52]	0.921	–	0.997	0.082	–
DeepV2D [22]	0.972	0.991	0.996	0.051	0.428
Ours-Large-scratch(DPT-Large)	**0.978**	**0.998**	**0.999**	**0.046**	**0.239**

can predict both robust and consistent disparity results, while other compared methods produce obvious artifacts and failure cases on these difficult scenes.

In both Fig. 7 and 8, one can observe that we produce much sharper estimation at edges, especially on skylines, which can be down to our rigorous annotation pipeline for VDW dataset, *e.g.*, the ensemble strategy for sky segmentation. Please refer to our supplementary document and demo video for more visual comparisons.

Table 4: **Influence of different training data**. (a) Training with different datasets. We conduct zero-shot evaluations on Sintel [40] with different training data for our NVDS$^+$ model. (b) Pretrain and finetune. Pretraining on our VDW can further improve the results on the closed-domain NYUDV2 [37], compared with training from scratch, even with weaker single-image depth predictors MiDaS-v2.1-Large [8] than DPT-Large [7].

Dataset	$\delta_1 \uparrow$	$OPW \downarrow$
NYUDV2	0.527	0.435
IRS+TartanAir	0.542	0.489
VDW(Ours)	**0.591**	**0.424**

(a) Different Training Data

Setting	$\delta_1 \uparrow$	$OPW \downarrow$
Scratch(DPT)	0.931	0.345
Pretrain(MiDaS)	0.941	0.347
Pretrain(DPT)	**0.950**	**0.339**

(b) Pretrain and Finetune

Influence of Training Data. The quality and diversity of data can greatly influence the learning-based video depth models. Our VDW dataset offers hundreds of times more data and scenes compared to previous works, which can be used to train robust learning-based models in the wild. To better show the difference, we compare our dataset with the existing datasets under zero-shot cross-dataset setting. As shown in Table 4 (a), we train our NVDS$^+$ with existing video depth datasets [37], [39], [41] and evaluate the model on Sintel [40] dataset. With both quantity and diversity, using VDW as the training data yields the best accuracy and consistency. Our VDW dataset is far more diverse for training robust video depth models, compared with large closed-domain dataset NYUDV2 [37] or synthetic natural-scene dataset like IRS [39] and TartanAir [41].

Moreover, although the proposed VDW is designed for natural scenes, it can also boost the performance on closed

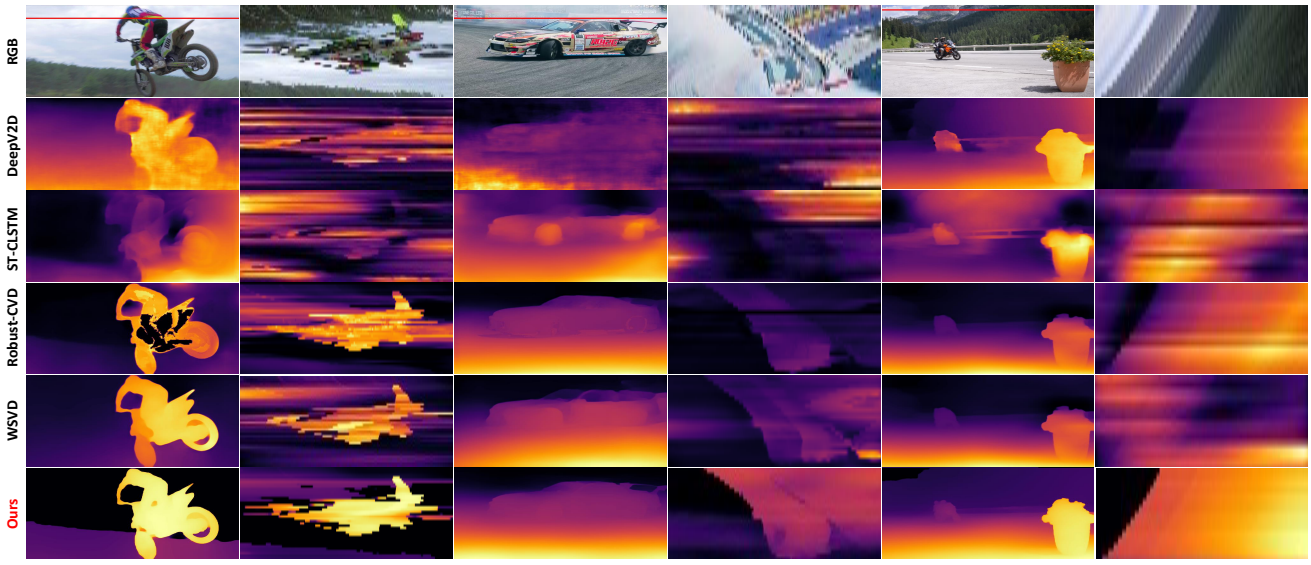


Figure 8: **Qualitative results on the DAVIS [77] dataset.** Our method can predict robust and consistent results on these challenging videos with large camera and object motions such as the motorcycle stunt flying over the hill and the drifting racing car, while other compared methods produce poor results or even failure cases on these difficult scenes.

Table 5: **Efficacy of the bidirectional inference strategy with flow-guided consistency fusion.** The simple bidirectional averaging can enlarge temporal receptive fields and improve the consistency beyond the forward or backward outcomes produced by the previous or post sliding window. Besides, temporal consistency can be further enhanced by our adaptive flow-guided fusion. We report the results on the VDW test set with DPT-Large [7] and MiDaS-v2.1-Large [8] as different depth predictors.

Method	$\delta_1 \uparrow$	$OPW \downarrow$
DPT-Large [7]	0.730	0.470
Pre-window	0.741	0.165
Post-window	0.741	0.174
Averaging	0.742	0.147
Flow-Guided	**0.742**	**0.129**

(a) DPT Initialization

Method	$\delta_1 \uparrow$	$OPW \downarrow$
MiDaS-Large [8]	0.651	0.676
Pre-window	0.700	0.207
Post-window	0.699	0.218
Averaging	0.700	0.180
Flow-Guided	**0.701**	**0.148**

(b) MiDaS Initialization

domains by serving as pretraining data. As in Table 4 (b), the VDW-pretrained model outperforms the model that is trained from scratch, even with weaker single-image model (MiDaS-v2.1-Large [8]). These results suggest that VDW can also benefit some closed-domain scenarios. This conclusion is also proved on the KITTI dataset [35] by comparing the quantitative results in the last row of Table 2 (Ours-Large) and Table 3 (Ours-Large-scratch).

5.3 Flow-Guided Consistency Fusion

Here, we conduct experiments to expound on the effectiveness of our bidirectional inference strategy with flow-guided consistency fusion. As shown in the first four rows of Table 5, whether using DPT [7] or MiDaS [8] as the single-image depth predictor, our NVDS$^+$ can already enforce the temporal consistency only with the previous or post sliding window of the target frame. Compared with the single-direction results, the bidirectional inference with simple averaging can improve the consistency by over 10.9% with larger temporal receptive fields.

Table 6: **Comparisons of FLOPs and model parameters.** We evaluate the efficiency of our NVDS$^+_{\textbf{Small}}$, NVDS$^+_{\textbf{Large}}$, and different depth predictors including DPT-Large [7], NeWCRFs [10], and MiDaS-v2.1-Large [8]. The FLOPs are evaluated on a 384×384 video sequence with four frames. The model parameters and FLOPs for NVDS$^+_{\textbf{Small}}$ and NVDS$^+_{\textbf{Large}}$ throughout the manuscript are in addition to the single-image depth predictors. Our lightweight NVDS$^+_{\textbf{Small}}$ model has 7 times fewer parameters and 17 times fewer FLOPs than NVDS$^+_{\textbf{Large}}$.

	DPT [7]	NeWCRFs [10]	MiDaS [8]	Ours-Large	Ours-Small
FLOPs (G)	1011.32	550.47	415.24	254.53	**35.51**
Params (M)	341.26	270.33	104.18	88.31	**5.04**

Besides, we propose the flow-guided consistency fusion paradigm to adaptively fuse the bidirectional disparity results of reference and target frames. With the flow-guided relevance maps and the adaptive fusion, the temporal consistency can be further enhanced. As shown in the last two rows of Table 5, compared with the simple averaging, our flow-guided consistency fusion can further improve the temporal consistency by 17.7%.

5.4 Efficiency Comparisons and Lightweight Model

Evaluations of Efficiency. For NVDS$^+_{\textbf{Large}}$, we compare the inference time on a 640×480 video with eight frames. The inference is conducted on one NVIDIA RTX A6000 GPU. As shown in Table 2, the proposed NVDS$^+_{\textbf{Large}}$ reduces the inference time by hundreds of times compared to the test-time-training-based CVD [18], Robust-CVD [19], and Zhang *et al.* [20]. The learning-based method DeepV2D [22] alternately estimates depth and camera poses, which is time-consuming. WSVD [42] is also slower than NVDS$^+_{\textbf{Large}}$.

We also compare the computational costs of the proposed NVDS$^+_{\textbf{Small}}$, NVDS$^+_{\textbf{Large}}$, and different depth predictors [7], [8], [10]. Model parameters and FLOPs are reported in Table 6. The FLOPs are evaluated on a 384×384 video



Figure 9: **Visual results of NVDS$^{+}_{\text{Small}}$ model.** We compare NVDS$^{+}_{\text{Small}}$ with lightweight depth predictors DPT-Swin2-Tiny [26] and MiDaS-v2.1-Small [8], along with the previous real-time video depth model ST-CLSTM [24]. Best view zoomed in on-screen for details.

Table 7: **Quantitative Comparisons of lightweight single-image depth predictors and video depth models on VDW.** We also report model parameters and the average FPS of processing all the testing videos with the input resolution of 896×384. The FPS numbers of our model include the initial depth predictors. Our NVDS$^{+}_{\text{Small}}$ shows both strong performance and high efficiency with different depth predictors.

Method	$\delta_1 \uparrow$	$\delta_2 \uparrow$	$\delta_3 \uparrow$	$Rel \downarrow$	$OPW \downarrow$	$FPS \uparrow$	Params $(M)\downarrow$
MiDaS-v2.1-Small [8]	0.564	0.794	0.891	0.401	0.652	**45.06**	21.48
DPT-Swin2-Tiny [26]	0.672	0.862	0.931	0.264	0.619	41.55	42.73
ST-CLSTM [24]	0.477	0.732	0.857	0.521	0.448	26.82	15.39
Ours-Small(MiDaS-v2.1-Small)	0.622	0.832	0.913	0.347	**0.236**	35.17	**5.04**
Ours-Small(DPT-Swin2-Tiny)	**0.704**	**0.881**	**0.944**	**0.251**	0.259	32.75	**5.04**

sequence with four frames. Our NVDS$^{+}_{\text{Large}}$ only incurs limited computation overhead compared with the depth predictors [7], [8], [10]. Besides, compared with NVDS$^{+}_{\text{Large}}$ model, our NVDS$^{+}_{\text{Small}}$ has 7 times fewer parameters and 17 times fewer FLOPs. As indicated in Table 7, our NVDS$^{+}_{\text{Small}}$ can achieve inference speeds of over 30 fps, surpassing the previous real-time video depth model ST-CLSTM [24].

Quantitative and Visual Results of NVDS$^{+}_{\text{Small}}$ model. We assess and compare the spatial accuracy and temporal consistency of lightweight single-image depth predictors and video depth models in Table 7. Collaborating with different lightweight depth predictors MiDaS-v2.1-Small [8] and DPT-Swin2-Tiny [26], our NVDS$^{+}_{\text{Small}}$ can improve the OPW by over 58.1% and δ_1 by over 3.2%. Meanwhile, NVDS$^{+}_{\text{Small}}$ maintains real-time processing of 35.17 fps and compact model structure only with $5.04M$ parameters.

Visual comparisons are shown in Fig. 9. NVDS$^{+}_{\text{Small}}$ achieves significant improvements over lightweight depth predictors [8], [26] and previous real-time ST-CLSTM [24] in both the spatial accuracy and temporal consistency.

5.5 Extension to Video Semantic Segmentation

In this section, we delve into the dataset, evaluation metrics, and experimental results of video semantic segmentation.

Table 8: **Comparisons of video semantic segmentation approaches on CityScapes [50] validation set.** Following SSLTM [46], all methods adopt ResNet-50 [72] as backbone.

Method	Params $(M)\downarrow$	mIoU$\uparrow$	TC$\uparrow$
ETC [43] (ECCV'20)	39.1	77.91	71.29
TMANet [47] (ICIP'21)	32.1	78.50	–
CFFM [32] (CVPR'22)	39.6	78.14	72.53
MRCFA [44] (ECCV'22)	39.2	78.12	72.21
IFR [45] (CVPR'22)	46.7	78.42	71.94
SSLTM [46] (CVPR'23)	43.1	79.69	–
Ours	42.7	**80.84**	**73.07**

Table 9: **Different semantic segmenters on CityScapes [50] validation set.** The results demonstrate the efficacy of our plug-and-play manner in video semantic segmentation.

	Initial		Ours	
	mIoU$\uparrow$	TC$\uparrow$	mIoU$\uparrow$	TC$\uparrow$
SegFormer-B1 [48]	77.87	70.32	79.91	72.94
SegFormer-B3 [48]	80.45	71.24	80.84	73.07
OneFormer [49]	**83.02**	**71.38**	**83.09**	**73.12**

5.5.1 *Dataset and Evaluation Metrics*

CityScapes Dataset. We follow previous single-image segmenters [48], [49] and video semantic segmentation approaches [32], [43], [44], [45], [46], [47] to conduct experiments and evaluations on CityScapes [50] dataset. CityScapes [50] is a widely-used standard benchmark for semantic segmentation. It contains videos with 30 frames and 17 fps of urban street scenes. The 20th frame of each video has high-quality annotations. A total of $5{,}000$ frames are finely annotated. In the training stage, we use the official training set with $2{,}975$ annotated frames as target frames.

Evaluation Metrics. To evaluate the accuracy of semantic segmentation on CityScapes [50] dataset, we adopt the mean Intersection over Union (mIoU) following prior arts [32], [43], [44], [45], [46], [47].

To evaluate the consistency of video results, previous methods [32], [43], [44], [46] mainly adopt the mean Video Consistency (mVC) [84] or the temporal consistency (TC) [43] metrics. However, the calculation of mVC requires annotations of all video frames, while CityScapes [50] only annotates one frame per video in both training and validation sets. Thus, we utilize the TC metric [43] for comparisons, which does not rely on segmentation ground truth. We denote the segmentation result of the nth frame as $\mathcal{Q}_n$. $\hat{\mathcal{Q}}_{n-1}$ represents the warped segmentation map from frame $n-1$ to frame n by optical flow [33]. TC [43] calculates mIoU between $\mathcal{Q}_n$ and $\hat{\mathcal{Q}}_{n-1}$ to measure the consistency:

$$TC = \frac{1}{N-1} \sum_{n=2}^{N} \frac{\mathcal{Q}_n \bigcap \hat{\mathcal{Q}}_{n-1}}{\mathcal{Q}_n \bigcup \hat{\mathcal{Q}}_{n-1}}. \tag{11}$$

Therefore, contrary to OPW for video depth, larger TC represents better consistency in the semantic segmentation maps. We report the average TC of all testing videos.

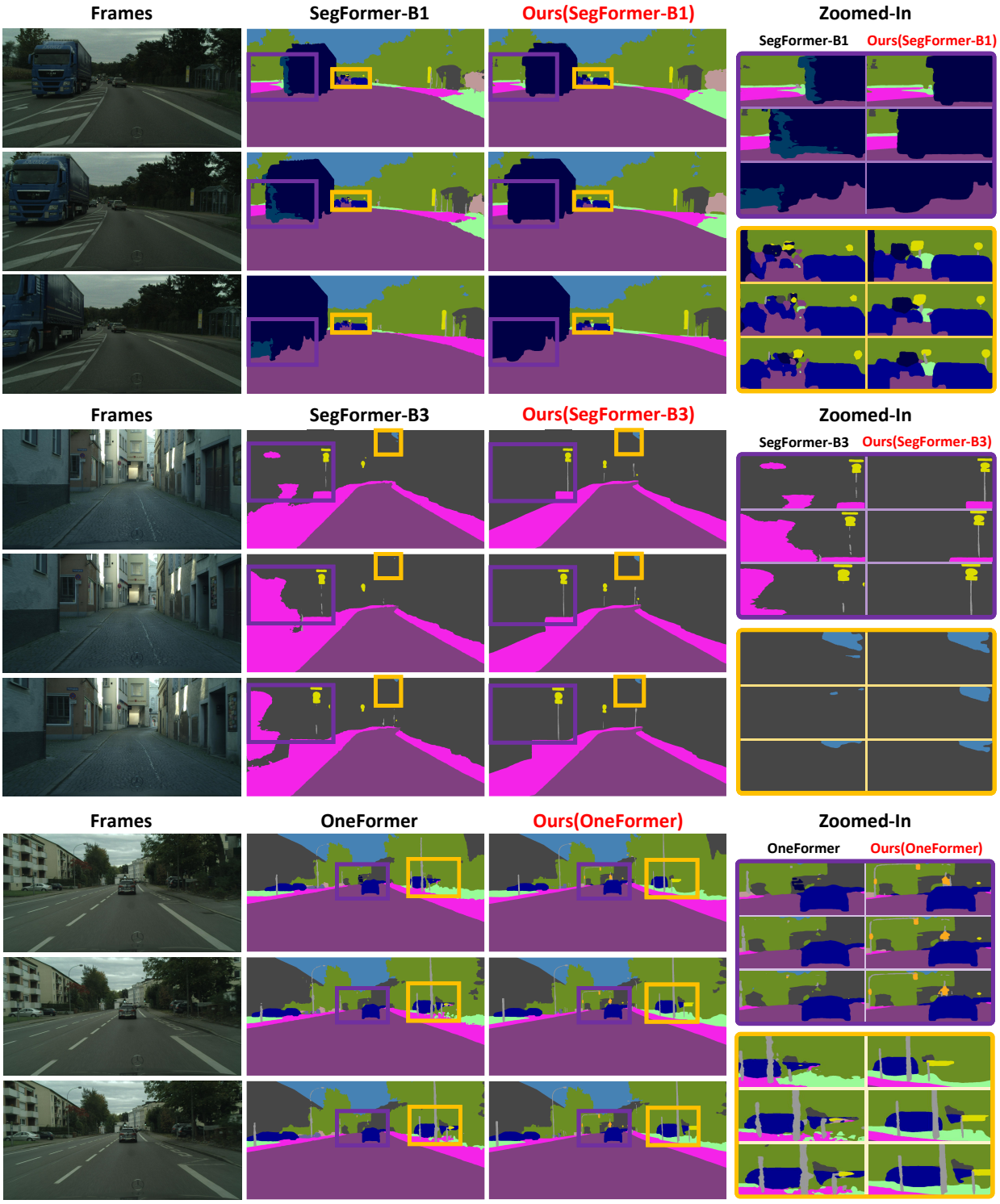


Figure 10: **Visual results of video semantic segmentation on CityScapes [50] dataset.** We compare NVDS+ with three different semantic segmenters SegFormer-B1, SegFormer-B3 [48], and OneFormer [49] to demonstrate the efficacy of our plug-and-play paradigm. Our NVDS+ can stabilize the temporal flickers in the initial segmentation maps. We highlight and zoom-in the regions with obvious difference in rectangular boxes. Best view zoomed in on-screen for details.

5.5.2 Comparisons with Prior Arts

Firstly, we compare our NVDS+ with the previous state-of-the-art video semantic segmentation approaches. The experimental results are shown in Table 8. We follow SSLTM [46] to use ResNet-50 [72] as the backbone for fair comparisons. With similar model parameters to prior arts [32], [43], [44], [45], [46], [47], our approach achieves state-of-the-art performance on both the segmentation accuracy and video consistency (mIoU and TC) for video semantic segmentation. The results prove the applicability and generality of our NVDS+ framework in video dense prediction.

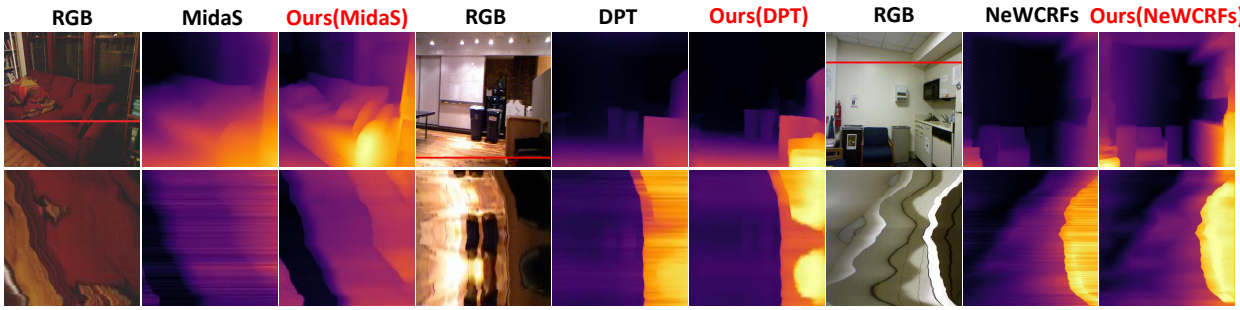


Figure 11: **Visual results on the NYUDV2 [37] dataset.** We compare $\text{NVDS}^{+}_{\textbf{Large}}$ with three different depth predictors, including the MiDaS-v2.1-Large [8], DPT-Large [7], and NeWCRFs [10].

Table 10: **Comparisons of different depth predictors on the NYUDV2 [37] dataset.** Our $\text{NVDS}^{+}_{\textbf{Large}}$ is compatible with different depth predictors in a plug-and-play manner.

	Initial			Ours		
	$\delta_1 \uparrow$	$Rel \downarrow$	$OPW \downarrow$	$\delta_1 \uparrow$	$Rel \downarrow$	$OPW \downarrow$
MiDaS-v2.1-Large [8]	0.910	0.095	0.862	0.941	0.076	0.373
DPT-Large [7]	0.928	0.084	0.811	0.950	0.072	0.364
NeWCRFs [10]	**0.937**	**0.072**	**0.645**	**0.957**	**0.068**	**0.326**

Table 11: **Temporal loss and inter-frame intervals l**. We randomly split 100 videos for training and 10 videos for testing from our VDW dataset in these two experiments.

Method	$\delta_1 \uparrow$	$OPW \downarrow$
DPT-Large [7]	0.621	0.492
$w/o\ \mathcal{L}^t$	**0.627**	0.303
$w/\ \mathcal{L}^t$	0.625	**0.216**

(a) Temporal Loss

Method	$\delta_1 \uparrow$	$OPW \downarrow$
$l = 1$	**0.625**	**0.216**
$l = 3$	0.618	0.219
$l = 5$	0.621	0.246

(b) Inter-frame Intervals

Table 12: **Baselines without NVDS⁺ stabilization network and reference frames numbers n**. The experiment is conducted on the same VDW subset as Table 11.

DPT w/	Single-frame	Multi-frame	**Ours**
$\delta_1 \uparrow$	0.615	0.608	**0.625**
$OPW \downarrow$	0.488	0.471	**0.216**

(a) W/o Stabilization Network

	n=1	n=2	**n=3**	n=4
$\delta_1 \uparrow$	0.618	0.622	**0.625**	**0.625**
$OPW \downarrow$	0.272	0.233	**0.216**	0.224

(b) Reference Frames

Table 13: **Forward training and backward inference.** The domain gap is modest and our model can handle it with minor impacts on the performance. Compared with training solely in the forward direction, bidirectional training only yields subtle improvements on the VDW dataset.

Inference	$\delta_1 \uparrow$	$OPW \downarrow$
Forward	0.741	0.165
Backward	0.741	0.174
Bidirectional	**0.742**	**0.129**

(a) Forward Training

Inference	$\delta_1 \uparrow$	$OPW \downarrow$
Forward	0.741	0.164
Backward	**0.742**	0.167
Bidirectional	**0.742**	**0.123**

(b) Bidirectional Training

Besides, we conduct evaluations to prove the effectiveness of our plug-and-play framework in video semantic segmentation. The quantitative results are presented in Table 9. We utilize three different initial semantic segmenters including SegFormer-B1, SegFormer-B3 [48], and OneFormer [49]. Our NVDS⁺ can enforce the temporal consistency over those different segmenters. Visual results are shown in Fig. 10. Regions with obvious improvements are highlighted and zoomed in by rectangular boxes. Our NVDS⁺ framework and pluggable paradigm showcase strong effectiveness in both video depth estimation and semantic segmentation tasks, proving the versatility and generality of our method.

5.6 Ablation Studies

Here we verify the effectiveness of the proposed method by ablation studies. We first ablate our plug-and-play paradigm with different depth predictors or semantic segmenters. Besides, We also discuss the temporal loss, the reference frames, and the baselines without the stabilization network.

Plug-and-play Manner. As shown in Table 10, we directly adapt our $\text{NVDS}^{+}_{\textbf{Large}}$ model to three different single-image depth models DPT-Large [7], MiDaS-v2.1-Large [8], and NeWCRFs [10]. For NeWCRFs [10], we adopt their official checkpoint on NYUDV2 [37]. By post-processing their initial flickering disparity maps, our NVDS⁺ achieves better temporal consistency and spatial accuracy. With higher initial depth accuracy, the spatial performance of our NVDS⁺ is also improved. The experiment demonstrates the effectiveness of our plug-and-play manner. Visual comparisons with those three depth predictors are shown in Fig. 11. Depth maps and scanline slice prove our accuracy and consistency.

On the other hand, in pursuit of real-time processing, our $\text{NVDS}^{+}_{\textbf{Small}}$ can cooperate with lightweight depth predictors in the pluggable paradigm, *e.g.*, MiDaS-v2.1-Small [8] and DPT-Swin2-Tiny [26]. As proved in Table 7, only with $5.04M$ model parameters, our $\text{NVDS}^{+}_{\textbf{Small}}$ can improve the consistency, accuracy, and achieve processing speeds of 35.17 fps. Qualitative comparisons with those lightweight depth predictors can be found in Fig. 9.

The plug-and-play manner can be effectively extended to video semantic segmentation. As shown in Table 9 and Fig. 10, with SegFormer-B1, SegFormer-B3 [48], and OneFormer [49] as segmenters, the temporal consistency and segmentation accuracy are both improved by NVDS⁺. With higher initial segmentation accuracy from OneFormer [49], the NVDS⁺ can also achieve better performance.

Temporal Loss. As in Table 11 (a), without the temporal loss as explicit supervision, our stabilization network can enforce temporal consistency. Adding the temporal loss can further remove flickers and improve temporal consistency.

Reference Frame Intervals. We denote the inter-frame intervals as l. As shown in Table 11 (b), $l = 1$ attains the best performance in our experiments.

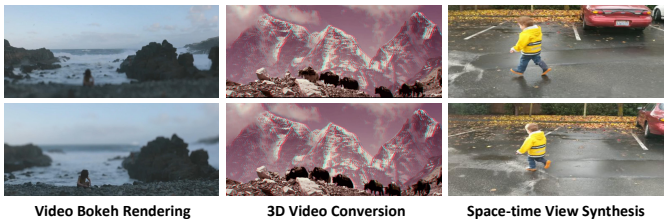


Figure 12: **Depth-based applications.** The consistent and accurate results from NVDS⁺ can be directly applied to various downstream video applications, *e.g.*, 3D video conversion [3], video bokeh rendering [1], [2], and space-time view synthesis [6], [85]. Best view zoomed in on-screen.



Figure 13: **Failure cases.** The analysis of failure cases could inspire future research avenues. In future work, more advanced techniques could be explored to enhance the robustness of video depth models against adverse lighting conditions, transparent surfaces, and specular reflections.

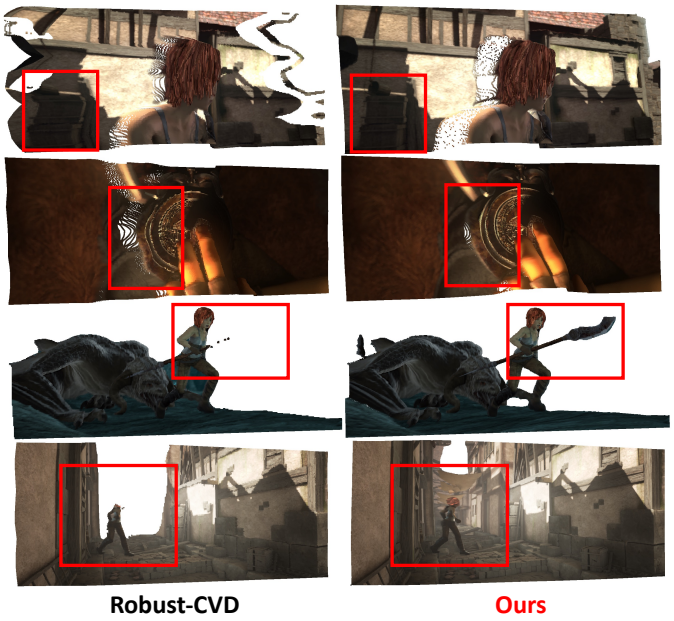


Figure 14: **Point cloud reconstructions.** Based on the videos of the Sintel dataset [40], we render the point clouds through Open3D [86] from a novel view point. We compare the reconstruction results of Robust-CVD [19] and our NVDS⁺. Due to the depth errors and artifacts produced by Robust-CVD [19], their reconstructions exhibit noticeable distortion, deformation, and structural incompleteness. In contrast, our NVDS⁺ framework can produce point clouds with better spatial geometry and structural integrity.

Reference Frame Numbers. As shown in Table 12 (b), using three reference frames (n=3) for a target frame achieves the best results. More reference frames (n=4) increase computational costs but bring no improvement, which can be caused by the temporal redundancy of videos. Overall, we adopt three reference frames with the inter-frame interval $l = 1$ for other experiments. The default setting works well for most videos. However, no single setting can be optimal for all videos. Different scenes, frame rates, objects, and motions in videos could all have an impact. For instance, we further discuss varied frame rates in the supplementary document.

Baselines without Stabilization Network. With DPT-Large [7] as the depth predictor, we train and evaluate two baselines without the stabilization network on the same subset as Table 11. We use the same temporal window as NVDS⁺. The first baseline (Single-frame) can only process each frame independently. Temporal window and loss $\mathcal{L}_t$ are used for consistency. The second baseline (Multi-frame) uses neighboring frames concatenated by channels to predict disparity of the target frame. Training and inference strategies are both kept the same as NVDS⁺. As shown in the Table 12 (a), temporal flickers cannot be solved by simply adding temporal windows and training loss on baselines. Proper designs are needed for inter-frame correlations. Our stabilization network improves consistency significantly.

Forward Training and Backward Inference. There exists a modest domain gap between forward training and backward inference. Certain scenarios that occur naturally in the forward direction, such as water spilling from a cup, cannot be realistically reversed to depict water returning to the cup. Nevertheless, given that a reversed video is intrinsically still a video, the domain gap has minor impacts on the model. As presented in Table 13, we compare the models trained on forward and bidirectional sequences. The subtle change in performance indicates that the model can handle this small domain gap. Bidirectional training would further escalate the training costs. Thus, considering the trade-off between performance and training burdens, we implement the main training process of all our models in the forward direction.

5.7 Depth-based Applications

With any in-the-wild monocular video and the disparity results predicted by our NVDS⁺, a multitude of downstream applications can be implemented. As shown in Fig. 12, we apply our disparity results to 3D video conversion [3], video bokeh rendering [1], [2], and space-time view synthesis [6], [85]. The consistent and robust predictions from NVDS⁺ can boost various depth-based applications.

Furthermore, depth maps serve as one of the bridges linking 2D and 3D spaces. Thus, merely verifying the performance of depth prediction is insufficient. It is also essential to carry out 3D reconstructions with integral and accurate spatial geometric structures, which can truly demonstrate the applicability of video depth models in 3D applications. As shown in Fig. 14, we utilize depth maps to reconstruct point clouds in 3D space. We compare the reconstruction results of Robust-CVD [19] and our NVDS⁺. The reconstructions from Robust-CVD [19] exhibit noticeable distortion, deformation, and structural incompleteness due to

their depth errors and artifacts. In contrast, our NVDS+ framework can produce point clouds with better spatial geometry and structural integrity. The results demonstrate the applicability of NVDS+ in the field of 3D vision.

5.8 Failure Cases

Our NVDS+ can seamlessly stabilize different depth predictors, predicting both consistent and accurate depth results. However, some drawbacks still exist. As shown in Fig. 13, several subtle failures occur in regions with adverse lighting conditions, such as the blurred contour of the dog at night, the depth error of the transparent window, and the incomplete tower tip under light overexposure.

These failures could be attributed to two factors. Firstly, depth errors from depth predictors affect NVDS+. Both DPT-Large [7] and NVDS+ produce unsatisfactory results in these areas. Additionally, the suboptimal predictions may result from inaccurate ground truth. The disparity annotated by optical flow [33], [61] is not entirely reliable for objects with specular reflections or transparency.

Analyzing these failure cases could inspire future research avenues to enhance the robustness of depth models against adverse lighting conditions, challenging weather, and transparent surfaces. Some recent attempts [87], [88], [89] have started to explore these directions. Overall, we aim to develop consistent video depth models with strong robustness and generality in various in-the-wild scenarios.

6 Conclusion

In this paper, we propose a NVDS+ framework and a large-scale natural-scene VDW dataset for video depth estimation. Different from previous learning-based video depth models that function as stand-alone models, our NVDS+ learns to stabilize the flickering results from the estimations of single-image depth models. In this way, NVDS+ can focus on the learning of temporal consistency, while inheriting the depth accuracy from the depth predictors without further tuning. We also elaborate on the VDW dataset to alleviate the data shortage. To our best knowledge, it is currently the largest video depth dataset in the wild. Besides, we also propose a bidirectional inference strategy with flow-guided consistency fusion to further improve temporal consistency by adaptively fusing forward and backward predictions. We instantiate a comprehensive model family with variants ranging from small to large scales to balance efficiency and performance. To further prove the versatility of our NVDS+ framework in video dense prediction and other downstream applications, we extend NVDS+ to video semantic segmentation and applications like bokeh rendering, novel view synthesis, and 3D reconstruction. We hope our work can serve as a solid baseline and provide a data foundation for the learning-based video dense prediction.

References

[1] J. Peng, Z. Cao, X. Luo, H. Lu, K. Xian, and J. Zhang, "Bokehme: When neural rendering meets classical rendering," in *Proceedings of the IEEE/CVF Conference on Computer Vision and Pattern Recognition (CVPR)*, 2022, pp. 16 283–16 292.

[2] X. Zhang, K. Matzen, V. Nguyen, D. Yao, Y. Zhang, and R. Ng, "Synthetic defocus and look-ahead autofocus for casual videography," *ACM Transactions on Graphics (TOG)*, vol. 38, no. 4, 2019.

[3] K. Karsch, C. Liu, and S. B. Kang, "Depth transfer: Depth extraction from video using non-parametric sampling," *IEEE transactions on pattern analysis and machine intelligence*, vol. 36, no. 11, pp. 2144–2158, 2014.

[4] X. Li, Z. Cao, H. Sun, J. Zhang, K. Xian, and G. Lin, "3d cinemagraphy from a single image," in *Proceedings of the IEEE/CVF Conference on Computer Vision and Pattern Recognition (CVPR)*, June 2023, pp. 4595–4605.

[5] X. Li, C. Hong, Y. Wang, Z. Cao, K. Xian, and G. Lin, "Symmnerf: Learning to explore symmetry prior for single-view view synthesis," in *Proceedings of the Asian Conference on Computer Vision (ACCV)*, December 2022, pp. 1726–1742.

[6] Z. Li, S. Niklaus, N. Snavely, and O. Wang, "Neural scene flow fields for space-time view synthesis of dynamic scenes," in *Proceedings of the IEEE/CVF Conference on Computer Vision and Pattern Recognition (CVPR)*, 2021, pp. 6498–6508.

[7] R. Ranftl, A. Bochkovskiy, and V. Koltun, "Vision transformers for dense prediction," in *Proceedings of the IEEE/CVF International Conference on Computer Vision (ICCV)*, 2021, pp. 12 179–12 188.

[8] R. Ranftl, K. Lasinger, D. Hafner, K. Schindler, and V. Koltun, "Towards robust monocular depth estimation: Mixing datasets for zero-shot cross-dataset transfer," *IEEE transactions on pattern analysis and machine intelligence*, vol. 44, no. 03, pp. 1623–1637, 2020.

[9] Y. Wang, X. Li, M. Shi, K. Xian, and Z. Cao, "Knowledge distillation for fast and accurate monocular depth estimation on mobile devices," in *Proceedings of the IEEE/CVF Conference on Computer Vision and Pattern Recognition (CVPR) Workshops*, June 2021, pp. 2457–2465.

[10] W. Yuan, X. Gu, Z. Dai, S. Zhu, and P. Tan, "Newcrfs: Neural window fully-connected crfs for monocular depth estimation," in *Proceedings of the IEEE/CVF Conference on Computer Vision and Pattern Recognition (CVPR)*, 2022, pp. 3916–3925.

[11] J. Li, Y. Wang, Z. Huang, J. Zheng, K. Xian, Z. Cao, and J. Zhang, "Diffusion-augmented depth prediction with sparse annotations," *arXiv preprint arXiv:2308.02283*, 2023.

[12] A. Saxena, M. Sun, and A. Y. Ng, "Make3d: Learning 3d scene structure from a single still image," *IEEE transactions on pattern analysis and machine intelligence*, vol. 31, no. 5, pp. 824–840, 2008.

[13] F. Liu, C. Shen, G. Lin, and I. Reid, "Learning depth from single monocular images using deep convolutional neural fields," *IEEE transactions on pattern analysis and machine intelligence*, vol. 38, no. 10, pp. 2024–2039, 2015.

[14] Z. Li and N. Snavely, "Megadepth: Learning single-view depth prediction from internet photos," in *Proceedings of the IEEE/CVF Conference on Computer Vision and Pattern Recognition (CVPR)*, June 2018.

[15] K. Xian, J. Zhang, O. Wang, L. Mai, Z. Lin, and Z. Cao, "Structure-guided ranking loss for single image depth prediction," in *Proceedings of the IEEE/CVF Conference on Computer Vision and Pattern Recognition (CVPR)*, 2020, pp. 608–617.

[16] K. Xian, C. Shen, Z. Cao, H. Lu, Y. Xiao, R. Li, and Z. Luo, "Monocular relative depth perception with web stereo data supervision," in *Proceedings of the IEEE/CVF Conference on Computer Vision and Pattern Recognition (CVPR)*, 2018, pp. 311–320.

[17] Z. Li, T. Dekel, F. Cole, R. Tucker, N. Snavely, C. Liu, and W. T. Freeman, "Mannequinchallenge: Learning the depths of moving people by watching frozen people," *IEEE transactions on pattern analysis and machine intelligence*, vol. 43, no. 12, pp. 4229–4241, 2020.

[18] X. Luo, J.-B. Huang, R. Szeliski, K. Matzen, and J. Kopf, "Consistent video depth estimation," *ACM Transactions on Graphics (ToG)*, vol. 39, no. 4, pp. 71–1, 2020.

[19] J. Kopf, X. Rong, and J.-B. Huang, "Robust consistent video depth estimation," in *Proceedings of the IEEE/CVF Conference on Computer Vision and Pattern Recognition (CVPR)*, 2021, pp. 1611–1621.

[20] Z. Zhang, F. Cole, R. Tucker, W. T. Freeman, and T. Dekel, "Consistent depth of moving objects in video," *ACM Transactions on Graphics (TOG)*, vol. 40, no. 4, pp. 1–12, 2021.

[21] J. L. Schönberger and J.-M. Frahm, "Structure-from-motion revisited," in *Proceedings of the IEEE/CVF Conference on Computer Vision and Pattern Recognition (CVPR)*, 2016, pp. 4104–4113.

[22] Z. Teed and J. Deng, "Deepv2d: Video to depth with differentiable structure from motion," in *International Conference on Learning Representations*, 2019.

[23] Y. Wang, Z. Pan, X. Li, Z. Cao, K. Xian, and J. Zhang, "Less is more: Consistent video depth estimation with masked frames modeling," in *Proceedings of the 30th ACM International Conference on Multimedia*, ser. MM '22. New York, NY, USA: Association for Computing Machinery, 2022, p. 6347–6358. [Online]. Available: https://doi.org/10.1145/3503161.3547978

[24] H. Zhang, C. Shen, Y. Li, Y. Cao, Y. Liu, and Y. Yan, "Exploiting temporal consistency for real-time video depth estimation," in *Proceedings of the IEEE/CVF International Conference on Computer Vision (ICCV)*, 2019, pp. 1725–1734.

[25] Y. Cao, Y. Li, H. Zhang, C. Ren, and Y. Liu, "Learning structure affinity for video depth estimation," in *Proceedings of the 29th ACM International Conference on Multimedia*, 2021, pp. 190–198.

[26] R. Birkl, D. Wofk, and M. Müller, "Midas v3. 1–a model zoo for robust monocular relative depth estimation," *arXiv preprint arXiv:2307.14460*, 2023.

[27] Y. Wang, M. Shi, J. Li, Z. Huang, Z. Cao, J. Zhang, K. Xian, and G. Lin, "Neural video depth stabilizer," in *Proceedings of the IEEE/CVF International Conference on Computer Vision (ICCV)*, 2023, pp. 9466–9476.

[28] A. Vaswani, N. Shazeer, N. Parmar, J. Uszkoreit, L. Jones, A. N. Gomez, Ł. Kaiser, and I. Polosukhin, "Attention is all you need," in *Advances in neural information processing systems*, vol. 30, 2017.

[29] J. Li, W. Wang, J. Chen, L. Niu, J. Si, C. Qian, and L. Zhang, "Video semantic segmentation via sparse temporal transformer," in *Proceedings of the 29th ACM International Conference on Multimedia*, ser. MM '21. New York, NY, USA: Association for Computing Machinery, 2021, p. 59–68. [Online]. Available: https://doi.org/10.1145/3474085.3475409

[30] Z. Liu, S. Luo, W. Li, J. Lu, Y. Wu, S. Sun, C. Li, and L. Yang, "Convtransformer: A convolutional transformer network for video frame synthesis," *arXiv preprint arXiv:2011.10185*, 2020.

[31] A. Arnab, M. Dehghani, G. Heigold, C. Sun, M. Lučić, and C. Schmid, "Vivit: A video vision transformer," in *Proceedings of the IEEE/CVF International Conference on Computer Vision (ICCV)*, 2021, pp. 6836–6846.

[32] G. Sun, Y. Liu, H. Ding, T. Probst, and L. Van Gool, "Coarse-to-fine feature mining for video semantic segmentation," in *Proceedings of the IEEE/CVF Conference on Computer Vision and Pattern Recognition (CVPR)*, 2022, pp. 3126–3137.

[33] H. Xu, J. Zhang, J. Cai, H. Rezatofighi, and D. Tao, "Gmflow: Learning optical flow via global matching," in *Proceedings of the IEEE/CVF Conference on Computer Vision and Pattern Recognition (CVPR)*, 2022, pp. 8121–8130.

[34] H. Xu, J. Zhang, J. Cai, H. Rezatofighi, F. Yu, D. Tao, and A. Geiger, "Unifying flow, stereo and depth estimation," *IEEE transactions on pattern analysis and machine intelligence*, 2023.

[35] A. Geiger, P. Lenz, C. Stiller, and R. Urtasun, "Vision meets robotics: The kitti dataset," *The International Journal of Robotics Research*, vol. 32, no. 11, pp. 1231–1237, 2013.

[36] J. Sturm, N. Engelhard, F. Endres, W. Burgard, and D. Cremers, "A benchmark for the evaluation of rgb-d slam systems," in *IEEE/RSJ International Conference on Intelligent Robots and Systems (IROS)*. IEEE, 2012, pp. 573–580.

[37] N. Silberman, D. Hoiem, P. Kohli, and R. Fergus, "Indoor segmentation and support inference from rgbd images," in *European Conference on Computer Vision (ECCV)*. Springer, 2012, pp. 746–760.

[38] A. Dai, A. X. Chang, M. Savva, M. Halber, T. Funkhouser, and M. Nießner, "Scannet: Richly-annotated 3d reconstructions of indoor scenes," in *Proceedings of the IEEE/CVF Conference on Computer Vision and Pattern Recognition (CVPR)*, 2017, pp. 5828–5839.

[39] Q. Wang, S. Zheng, Q. Yan, F. Deng, K. Zhao, and X. Chu, "Irs: A large naturalistic indoor robotics stereo dataset to train deep models for disparity and surface normal estimation," in *IEEE International Conference on Multimedia and Expo (ICME)*. IEEE Computer Society, 2021, pp. 1–6.

[40] D. J. Butler, J. Wulff, G. B. Stanley, and M. J. Black, "A naturalistic open source movie for optical flow evaluation," in *European Conference on Computer Vision (ECCV)*. Springer, 2012, pp. 611–625.

[41] W. Wang, D. Zhu, X. Wang, Y. Hu, Y. Qiu, C. Wang, Y. Hu, A. Kapoor, and S. Scherer, "Tartanair: A dataset to push the limits of visual slam," in *IEEE/RSJ International Conference on Intelligent Robots and Systems (IROS)*. IEEE, 2020, pp. 4909–4916.

[42] C. Wang, S. Lucey, F. Perazzi, and O. Wang, "Web stereo video supervision for depth prediction from dynamic scenes," in *IEEE International Conference on 3D Vision (3DV)*. IEEE, 2019, pp. 348–357.

[43] Y. Liu, C. Shen, C. Yu, and J. Wang, "Efficient semantic video segmentation with per-frame inference," in *European Conference on Computer Vision (ECCV)*. Springer, 2020, pp. 352–368.

[44] G. Sun, Y. Liu, H. Tang, A. Chhatkuli, L. Zhang, and L. Van Gool, "Mining relations among cross-frame affinities for video semantic segmentation," in *European Conference on Computer Vision (ECCV)*. Springer, 2022, pp. 522–539.

[45] J. Zhuang, Z. Wang, and Y. Gao, "Semi-supervised video semantic segmentation with inter-frame feature reconstruction," in *Proceedings of the IEEE/CVF Conference on Computer Vision and Pattern Recognition (CVPR)*, 2022, pp. 3263–3271.

[46] J. Lao, W. Hong, X. Guo, Y. Zhang, J. Wang, J. Chen, and W. Chu, "Simultaneously short-and long-term temporal modeling for semi-supervised video semantic segmentation," in *Proceedings of the IEEE/CVF Conference on Computer Vision and Pattern Recognition (CVPR)*, 2023, pp. 14 763–14 772.

[47] H. Wang, W. Wang, and J. Liu, "Temporal memory attention for video semantic segmentation," in *IEEE International Conference on Image Processing (ICIP)*, 2021, pp. 2254–2258.

[48] E. Xie, W. Wang, Z. Yu, A. Anandkumar, J. M. Alvarez, and P. Luo, "Segformer: Simple and efficient design for semantic segmentation with transformers," *Advances in neural information processing systems*, vol. 34, pp. 12 077–12 090, 2021.

[49] J. Jain, J. Li, M. T. Chiu, A. Hassani, N. Orlov, and H. Shi, "Oneformer: One transformer to rule universal image segmentation," in *Proceedings of the IEEE/CVF Conference on Computer Vision and Pattern Recognition (CVPR)*, 2023, pp. 2989–2998.

[50] M. Cordts, M. Omran, S. Ramos, T. Rehfeld, M. Enzweiler, R. Benenson, U. Franke, S. Roth, and B. Schiele, "The cityscapes dataset for semantic urban scene understanding," in *Proceedings of the IEEE/CVF Conference on Computer Vision and Pattern Recognition (CVPR)*, 2016, pp. 3213–3223.

[51] J. L. Schönberger, E. Zheng, M. Pollefeys, and J.-M. Frahm, "Pixelwise view selection for unstructured multi-view stereo," in *European Conference on Computer Vision (ECCV)*, vol. 9907, 2016, pp. 501–518.

[52] P. Ruhkamp, D. Gao, H. Chen, N. Navab, and B. Busam, "Attention meets geometry: Geometry guided spatial-temporal attention for consistent self-supervised monocular depth estimation," in *IEEE International Conference on 3D Vision (3DV)*. IEEE, 2021, pp. 837–847.

[53] G. Hinton, O. Vinyals, J. Dean *et al.*, "Distilling the knowledge in a neural network," *arXiv preprint arXiv:1503.02531*, 2015.

[54] Y. Liu, K. Chen, C. Liu, Z. Qin, Z. Luo, and J. Wang, "Structured knowledge distillation for semantic segmentation," in *Proceedings of the IEEE/CVF Conference on Computer Vision and Pattern Recognition (CVPR)*, 2019, pp. 2604–2613.

[55] N. Khan, E. Penner, D. Lanman, and L. Xiao, "Temporally consistent online depth estimation using point-based fusion," in *Proceedings of the IEEE/CVF Conference on Computer Vision and Pattern Recognition (CVPR)*, 2023, pp. 9119–9129.

[56] Z. Li, W. Ye, D. Wang, F. X. Creighton, R. H. Taylor, G. Venkatesh, and M. Unberath, "Temporally consistent online depth estimation in dynamic scenes," in *Proceedings of the IEEE/CVF winter conference on applications of computer vision (WACV)*, 2023, pp. 3018–3027.

[57] K. Xian, J. Peng, Z. Cao, J. Zhang, and G. Lin, "Vita: Video transformer adaptor for robust video depth estimation," *IEEE Transactions on Multimedia*, 2023.

[58] R. Yasarla, H. Cai, J. Jeong, Y. Shi, R. Garrepalli, and F. Porikli, "Mamo: Leveraging memory and attention for monocular video depth estimation," in *Proceedings of the IEEE/CVF International Conference on Computer Vision (ICCV)*, 2023, pp. 8754–8764.

[59] Y. Liu, C. Shu, J. Wang, and C. Shen, "Structured knowledge distillation for dense prediction," *IEEE transactions on pattern analysis and machine intelligence*, 2020.

[60] Z. Liu, H. Hu, Y. Lin, Z. Yao, Z. Xie, Y. Wei, J. Ning, Y. Cao, Z. Zhang, L. Dong *et al.*, "Swin transformer v2: Scaling up capacity and resolution," in *Proceedings of the IEEE/CVF Conference on Computer Vision and Pattern Recognition (CVPR)*, 2022, p. 12009.

[61] E. Ilg, N. Mayer, T. Saikia, M. Keuper, A. Dosovitskiy, and T. Brox, "Flownet 2.0: Evolution of optical flow estimation with deep networks," in *Proceedings of the IEEE/CVF Conference on Computer Vision and Pattern Recognition (CVPR)*, 2017, pp. 2462–2470.

[62] N. Bonneel, J. Tompkin, K. Sunkavalli, D. Sun, S. Paris, and

H. Pfister, "Blind video temporal consistency," *ACM Transactions on Graphics (TOG)*, vol. 34, no. 6, 2015.

[63] W.-S. Lai, J.-B. Huang, O. Wang, E. Shechtman, E. Yumer, and M.-H. Yang, "Learning blind video temporal consistency," in *European Conference on Computer Vision (ECCV)*. Springer, 2018, pp. 170–185.

[64] C. Lei, Y. Xing, H. Ouyang, and Q. Chen, "Deep video prior for video consistency and propagation," *IEEE transactions on pattern analysis and machine intelligence*, vol. 45, no. 1, pp. 356–371, 2022.

[65] S. Hochreiter and J. Schmidhuber, "Long short-term memory," *Neural computation*, vol. 9, no. 8, pp. 1735–1780, 1997.

[66] C. Lei, X. Ren, Z. Zhang, and Q. Chen, "Blind video deflickering by neural filtering with a flawed atlas," in *Proceedings of the IEEE/CVF Conference on Computer Vision and Pattern Recognition (CVPR)*, 2023, pp. 10 439–10 448.

[67] A. Dosovitskiy, L. Beyer, A. Kolesnikov, D. Weissenborn, X. Zhai, T. Unterthiner, M. Dehghani, M. Minderer, G. Heigold, S. Gelly *et al.*, "An image is worth 16x16 words: Transformers for image recognition at scale," in *International Conference on Learning Representations*, 2020.

[68] G. Lin, A. Milan, C. Shen, and I. Reid, "Refinenet: Multi-path refinement networks for high-resolution semantic segmentation," in *Proceedings of the IEEE/CVF Conference on Computer Vision and Pattern Recognition (CVPR)*, 2017, pp. 1925–1934.

[69] T.-Y. Lin, P. Dollár, R. Girshick, K. He, B. Hariharan, and S. Belongie, "Feature pyramid networks for object detection," in *Proceedings of the IEEE/CVF Conference on Computer Vision and Pattern Recognition (CVPR)*, 2017, pp. 2117–2125.

[70] G. Fang, X. Ma, M. Song, M. B. Mi, and X. Wang, "DepGraph: Towards any structural pruning," in *Proceedings of the IEEE/CVF Conference on Computer Vision and Pattern Recognition (CVPR)*, 2023, pp. 16 091–16 101.

[71] B. Zhou, H. Zhao, X. Puig, S. Fidler, A. Barriuso, and A. Torralba, "Scene parsing through ADE20K dataset," in *Proceedings of the IEEE/CVF Conference on Computer Vision and Pattern Recognition (CVPR)*, 2017, pp. 633–641.

[72] K. He, X. Zhang, S. Ren, and J. Sun, "Deep residual learning for image recognition," in *Proceedings of the IEEE/CVF Conference on Computer Vision and Pattern Recognition (CVPR)*, 2016, pp. 770–778.

[73] J. Deng, W. Dong, R. Socher, L.-J. Li, K. Li, and L. Fei-Fei, "ImageNet: A large-scale hierarchical image database," in *Proceedings of the IEEE/CVF Conference on Computer Vision and Pattern Recognition (CVPR)*, 2009, pp. 248–255.

[74] P. Li, Y. Ding, L. Li, J. Guan, and Z. Li, "Towards practical consistent video depth estimation," in *Proceedings of the 2023 ACM International Conference on Multimedia Retrieval*, 2023, pp. 388–397.

[75] B. Cheng, I. Misra, A. G. Schwing, A. Kirillov, and R. Girdhar, "Masked-attention mask transformer for universal image segmentation," in *Proceedings of the IEEE/CVF Conference on Computer Vision and Pattern Recognition (CVPR)*, 2022, pp. 1290–1299.

[76] VDW Dataset Toolkits developers, "VDW Dataset Toolkits," https://github.com/RaymondWang987/VDW_Dataset_Toolkits, [Online; Accessed 2024].

[77] J. Pont-Tuset, F. Perazzi, S. Caelles, P. Arbeláez, A. Sorkine-Hornung, and L. Van Gool, "The 2017 DAVIS challenge on video object segmentation," *arXiv preprint arXiv:1704.00675*, 2017.

[78] D. Eigen, C. Puhrsch, and R. Fergus, "Depth map prediction from a single image using a multi-scale deep network," in *Advances in neural information processing systems*, vol. 27, 2014, pp. 2366–2374.

[79] J. Wang, Y. Zhong, Y. Dai, S. Birchfield, K. Zhang, N. Smolyanskiy, and H. Li, "Deep two-view structure-from-motion revisited," in *Proceedings of the IEEE/CVF Conference on Computer Vision and Pattern Recognition (CVPR)*, 2021, pp. 8953–8962.

[80] S. Zhu and X. Liu, "Lighteddepth: Video depth estimation in light of limited inference view angles," in *Proceedings of the IEEE/CVF Conference on Computer Vision and Pattern Recognition (CVPR)*, 2023, pp. 5003–5012.

[81] J.-W. Bian, H. Zhan, N. Wang, Z. Li, L. Zhang, C. Shen, M.-M. Cheng, and I. Reid, "Unsupervised scale-consistent depth learning from video," *International Journal of Computer Vision (IJCV)*, 2021.

[82] J.-W. Bian, H. Zhan, N. Wang, T.-J. Chin, C. Shen, and I. Reid, "Auto-rectify network for unsupervised indoor depth estimation," *IEEE transactions on pattern analysis and machine intelligence*, vol. 44, no. 12, pp. 9802–9813, 2022.

[83] L. Sun, J.-W. Bian, H. Zhan, W. Yin, I. Reid, and C. Shen, "Sc-depthv3: Robust self-supervised monocular depth estimation for dynamic scenes," *IEEE transactions on pattern analysis and machine intelligence*, 2023.

[84] J. Miao, Y. Wei, Y. Wu, C. Liang, G. Li, and Y. Yang, "Vspw: A large-scale dataset for video scene parsing in the wild," in *Proceedings of the IEEE/CVF Conference on Computer Vision and Pattern Recognition (CVPR)*, 2021, pp. 4133–4143.

[85] Z. Li, Q. Wang, F. Cole, R. Tucker, and N. Snavely, "Dynibar: Neural dynamic image-based rendering," in *Proceedings of the IEEE/CVF Conference on Computer Vision and Pattern Recognition (CVPR)*, 2023, pp. 4273–4284.

[86] Q.-Y. Zhou, J. Park, and V. Koltun, "Open3d: A modern library for 3d data processing," *arXiv preprint arXiv:1801.09847*, 2018.

[87] S. Gasperini, N. Morbitzer, H. Jung, N. Navab, and F. Tombari, "Robust monocular depth estimation under challenging conditions," in *Proceedings of the IEEE/CVF International Conference on Computer Vision (ICCV)*, 2023, pp. 8177–8186.

[88] K. Saunders, G. Vogiatzis, and L. J. Manso, "Self-supervised monocular depth estimation: Let's talk about the weather," in *Proceedings of the IEEE/CVF International Conference on Computer Vision (ICCV)*, 2023, pp. 8907–8917.

[89] P. Z. Ramirez, F. Tosi, L. Di Stefano, R. Timofte, A. Costanzino, M. Poggi, S. Salti, S. Mattoccia, Y. Zhang, C. Wu, Z. He, S. Yin, J. Dong, Y. Liu, H. Jiang, J. Shi, Y. A, Y. Jin, D. Li, B. Ke, A. Obukhov, T. Wang, N. Metzger, S. Huang, K. Schindler, Y. Huang, J. Li, J. Zhang, Y. Wang, Z. Huang, T. Liu, Z. Cao, P. Li, J.-L. Wang, W. Zhu, H. Geng, Y. Zhang, L. Lan, K. Xu, T. Sun, Q. Xu, S. Saini, A. Gupta, S. K. Mistry, A. Shukla, V. Jakhetiya, S. Jaiswal, Y. Sun, Z. Zheng, Y. Ning, J.-H. Cheng, H.-I. Liu, H.-W. Huang, C.-Y. Yang, Z. Jiang, Y.-H. Peng, A. Huang, and J.-N. Hwang, "Ntire challenge on hr depth from images of specular and transparent surfaces," in *Proceedings of the IEEE/CVF Conference on Computer Vision and Pattern Recognition (CVPR) Workshops*, 2024, pp. 6499–6512.

[90] Creative Commons organization, "Creative Commons Attribution-NonCommercial-ShareAlike 4.0 International," https://creativecommons.org/licenses/by-nc-sa/4.0/legalcode.

[91] FFmpeg developers, "FFmpeg," https://ffmpeg.org, [Online; Accessed 2022].

[92] PySceneDetect developers, "PySceneDetect," http://scenedetect.com, [Online; Accessed 2022].

[93] S. R. Bulo, L. Porzi, and P. Kontschieder, "In-place activated batchnorm for memory-optimized training of dnns," in *Proceedings of the IEEE/CVF Conference on Computer Vision and Pattern Recognition (CVPR)*, 2018, pp. 5639–5647.

[94] S. Meister, J. Hur, and S. Roth, "Unflow: Unsupervised learning of optical flow with a bidirectional census loss," in *Proceedings of the AAAI conference on artificial intelligence*, vol. 32, no. 1, 2018.

[95] S. Xie, R. Girshick, P. Dollár, Z. Tu, and K. He, "Aggregated residual transformations for deep neural networks," in *Proceedings of the IEEE/CVF Conference on Computer Vision and Pattern Recognition (CVPR)*, 2017, pp. 1492–1500.

[96] H. Fan, B. Xiong, K. Mangalam, Y. Li, Z. Yan, J. Malik, and C. Feichtenhofer, "Multiscale vision transformers," in *Proceedings of the IEEE/CVF International Conference on Computer Vision (ICCV)*, 2021, pp. 6824–6835.

[97] H. Zhang, C. Wu, Z. Zhang, Y. Zhu, H. Lin, Z. Zhang, Y. Sun, T. He, J. Mueller, R. Manmatha *et al.*, "Resnest: Split-attention networks," *arXiv preprint arXiv:2004.08955*, 2020.

[98] L. Wang, X. Shen, J. Zhang, O. Wang, Z. Lin, C.-Y. Hsieh, S. Kong, and H. Lu, "Deeplens: shallow depth of field from a single image," *ACM Transactions on Graphics (TOG)*, vol. 37, no. 6, 2018.

[99] Camocomp developers, "CAmera MOtion COMPensation," https://github.com/daien/camocomp, [Online; Accessed 2024].



Yiran Wang received the B.S. degree from Huazhong University of Science and Technology, Wuhan, China, in 2021. He is currently pursuing the Ph.D. degree with the School of Artificial Intelligence and Automation, Huazhong University of Science and Technology, Wuhan, China. His research interests include computer vision and pattern recognition, with particular emphasis on depth estimation, video consistency, dense prediction, and 3D vision.



Min Shi received the B.S. degree and M.S. degree from the School of Artificial Intelligence and Automation, Huazhong University of Science and Technology, China. He is interested in computer vision and deep learning, few-shot learning, multi-modal models, and 3D vision.



Jiaqi Li received the B.S. degree from Huazhong University of Science and Technology, Wuhan, China, in 2023. He is currently pursuing the M.S. degree with the School of Artificial Intelligence and Automation, Huazhong University of Science and Technology, Wuhan, China. His research interests lie in 3D Vision, with particular emphasis on monocular and multi-view depth estimation.



Chaoyi Hong received the B.S. degree from Huazhong University of Science and Technology, Wuhan, China, in 2019. She is pursuing a Ph.D. degree with the School of Artificial Intelligence and Automation, Huazhong University of Science and Technology. Her research interests include computer vision and deep learning, focusing on dense prediction and aesthetics-related tasks, particularly on image matting and image cropping.



Zihao Huang received the B.S. degree from Huazhong University of Science and Technology, Wuhan, China, in 2023. He is currently pursuing the M.S. degree with the School of Artificial Intelligence and Automation, Huazhong University of Science and Technology, Wuhan, China. His research interests mainly include 3D avatar creation, focusing on fast and high-quality 3D human reconstructions.



Juewen Peng received the B.S. and M.S. degrees from the School of Artificial Intelligence and Automation, Huazhong University of Science and Technology. He is currently pursuing the Ph.D. degree in the College of Computing and Data Science, Nanyang Technological University, Singapore. His research interests include computational photography, bokeh rendering, image deblurring, and 3D vision.



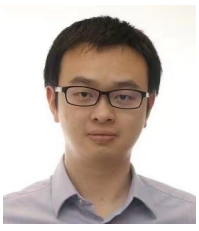
Zhiguo Cao (Member, IEEE) is currently a Professor with the School of Artificial Intelligence and Automation, Huazhong University of Science and Technology. His research interests spread across computational photography, monocular depth estimation, 3d video processing, motion detection, and human action analysis. He has published dozens of papers in international journals and prominent conferences.



Jianming Zhang received the B.S. and M.S. degrees in mathematics from Tsinghua University, Beijing, China, in 2008 and 2011, respectively, and the Ph.D. degree in computer science from Boston University, Boston, Massachusetts, in 2016. He is a principal research scientist at Adobe. His research interests include visual saliency, image segmentation, 3D understanding, and generative models.



Ke Xian received the B.S. and Ph.D. degrees from Huazhong University of Science and Technology (HUST), China. From August 2016 to September 2017, he worked as a joint training Ph.D. student with the University of Adelaide, Australia. From October 2021 to November 2023, he worked as a Research Fellow with the S-Lab, Nanyang Technological University (NTU), Singapore. Now, he is a lecturer with the School of Electronic Information and Communications, Huazhong University of Science and Technology. His research interests include robust 3D vision, 2D scene understanding, and computational photography.



Guosheng Lin is an Associate Professor at the College of Computing and Data Science, Nanyang Technological University, Singapore. He received his Ph.D. degree from The University of Adelaide in 2014. His research interests are in computer vision and machine learning including scene understanding, 3D vision and generative learning.

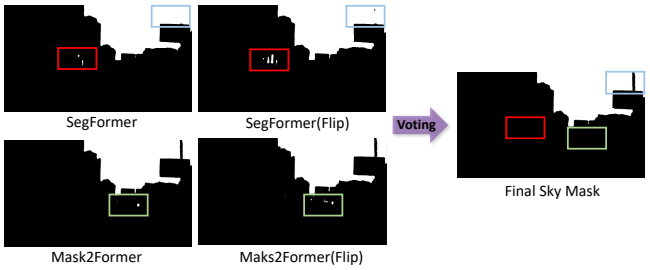


Figure 15: **Model ensemble strategy for sky segmentation on VDW dataset.** White area represents sky regions. Errors and noises in the rectangles are removed by model ensemble and voting, which improves the quality of the ground truth.

APPENDIX A
MORE DETAILS ON THE VDW DATASET

A.1 Releasing of the VDW Dataset.

We have released the VDW dataset under strict conditions. We must ensure that the release won't violate any copyright requirements. To this end, we will not release any video frames or the derived data in public. Instead, we provide metadata and detailed toolkits, which can be used to reproduce VDW or generate your own data. All the metadata and toolkits are licensed under CC BY-NC-SA 4.0 [90], which can only be used for academic and research purposes. Refer to the VDW website https://raymondwang987.github.io/VDW/ for more information.

A.2 Dataset Construction

Data Acquisition and Pre-processing. Here we add more details on data acquisition and pre-processing (Sec. 4, page 7, main paper). Having obtained the raw videos, we use FFmpeg [91] and PySceneDetect [92] to split all the videos into 104,582 sequences. We manually check and remove the duplicated, chaotic, and blur scenes. Videos that are wrongly split by the scene detect tools are also removed. Finally, we reserve 32,405 videos with more than six million frames for disparity annotation.

Disparity Annotation. In Sec. 4 of the main paper, we mentioned that the disparity ground truth is obtained via sky segmentation and optical flow estimation. Here we specify the details. Compared with common practice [8], [16], we introduce a few engineering improvements to make the disparity maps more accurate. As the sky is considered to be infinitely far, pixels in the sky regions should be segmented and set to the minimum value in the disparity maps. We find that using a single segmentation model [68], [93] like prior arts [8], [16] causes errors and noises in the sky regions. Hence, we generate the sky masks in a model ensemble manner. Each frame along with its horizontally flipped copy are fed into two state-of-the-art semantic segmentation models SegFormer [48] and Mask2Former [75], which yields four sky masks in total. A pixel is considered as the sky when it is positive in more than two predicted sky masks. Besides, we also fill the connected regions with less than 50 pixels to further remove the noisy holes in the sky masks. Such ensemble strategy can improve the quality of the ground truth as shown in Fig. 15, and consequently improves the performance of the trained models, especially on skylines as shown in Fig. 22.

Following the practice of previous single-image depth datasets [8], [16], we adopt a state-of-the-art optical flow model GMFlow [33] to generate the ground truth disparity of the left- and right-eye views. The estimated optical flow is bidirectional. We perform a consistency check between the optical flow pairs to obtain the valid masks for training. We adopt the adaptive consistency threshold for each pixel as [94]. The ground truth of each video is normalized by its minimum and maximum disparity. Then, the disparity value is discretized into 65,535 intervals. Fig. 17 shows more examples of our VDW dataset.

Invalid Sample Filtering. Having obtained the annotations, we further filter the videos that are not qualified for our dataset. According to optical flow and valid masks, samples with the following three conditions are removed: 1) more than 30% of pixels in the consistency masks are invalid; 2) more than 10% of pixels have vertical disparity larger than two pixels; 3) the average range of horizontal disparity is less than 15 pixels. Then, we manually check all the videos along with their corresponding ground truth, and remove the samples with obvious errors. Finally, we retain 14,203 videos with 2,237,320 frames in VDW dataset.

Table 14: **Video and frame numbers statistics of VDW training set.** Our VDW dataset contains 14,203 videos from movies, animations, documentaries, and web videos.

Sources	Titles	Videos	Frames
Documentaries	Deepsea Challenge	210	38,078
	Kingdom of Plants	253	95,742
	Little Monsters	242	50,420
	Jerusalem	37	21,574
Animations	Coco	1,079	146,002
	Kung Fu Panda 3	959	68,405
Movies	Exodus: Gods and Kings	1,339	99,146
	Geostorm	857	52,028
	Hugo	301	25,091
	Mission: Impossible-Fallout	664	46,344
	Noah	1,160	85,161
	Pompeii	158	10,112
	Spider-Man: No Way Home	914	75,077
	The Legend of Tarzan	735	64,840
	The Three Musketeers	253	18,180
	Gravity	191	38,332
	Silent Hill 2	72	5,076
	Transformers: Age of Extinction	1,323	84,619
	Doctor Strange	299	23,779
	Battle of the Year	454	19,613
	Justice League	428	37,202
	The Hobbit 2	644	53,391
	The Great Gatsby	729	49,079
	Billy Lynn's Long Halftime Walk	242	29,137
Web Videos	YouTube	514	40,897
	bilibili	146	17,243
All	–	14,203	2,237,320

Table 15: **Video and frame numbers statistics of VDW test set.** VDW test set adopts different data sources from training data, *i.e.*, different movies, web videos, or animations.

Sources	Titles	Videos	Frames
Movies	Eternals	39	4,802
	Everest	17	2,922
	Fantastic Beasts and Where to Find Them	17	27,27
Animation	Frozen 2	10	1,098
Web Videos	bilibili	7	1,073
All	–	90	12,622

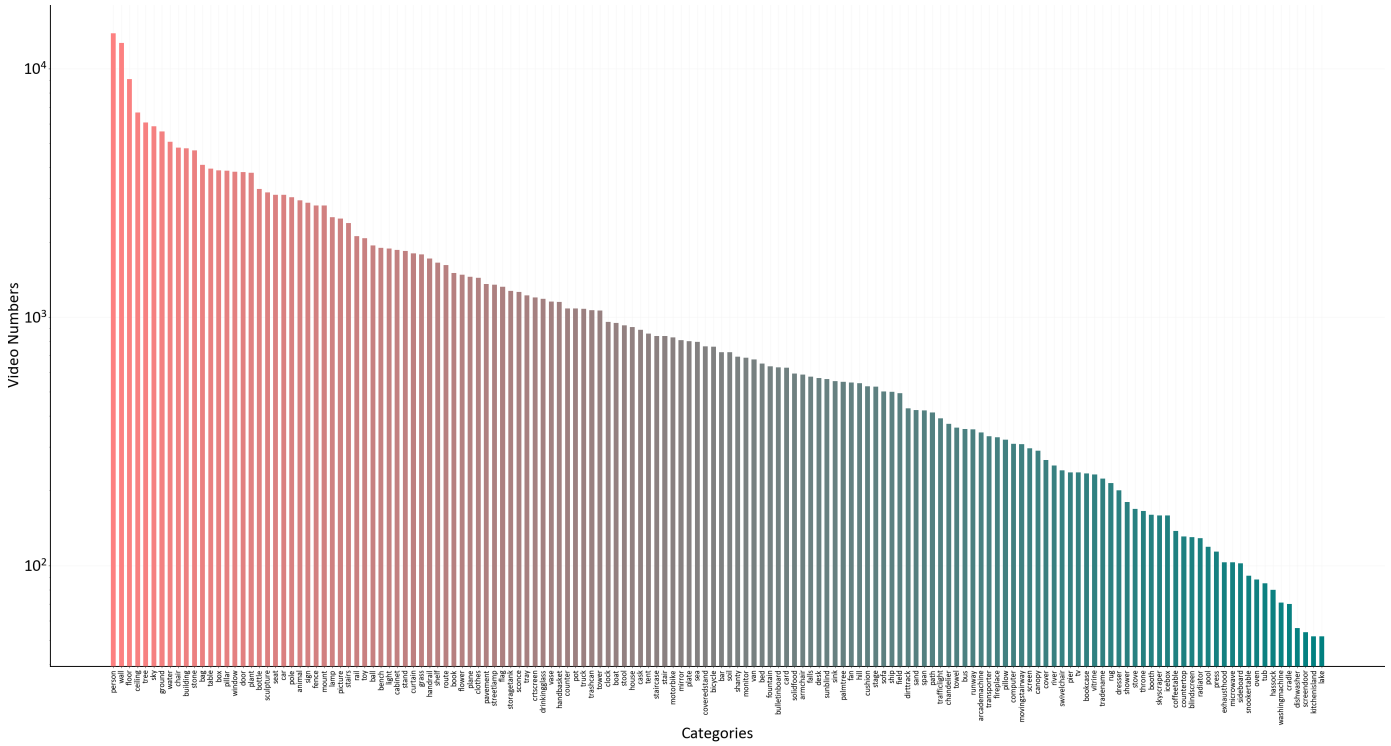


Figure 16: The statistics of the 150 semantic categories in VDW dataset.

A.3 Data Statistics

Data Sources. Taking over 6 months to process, VDW training set contains 14,203 videos with 2,237,320 frames. The detailed data sources of training set and test set are listed in Table 14 and Table 15 respectively.

Frame Rates and Frame Numbers. For all our sequences, the lowest frame rate is 12 fps, the highest frame rate is 60 fps, and the average frame rate is 28.92 fps. Even some special videos, such as fast-forward or slow-motion sequences, are included in the VDW dataset. The minimum frame number is 18 while the maximum is 8,005.

Objects Presented in the VDW Dataset. To verify the diversity of objects in our videos. We conduct semantic segmentation with Mask2Former [75] trained on ADE20K [71]. All the 150 categories are covered in our dataset. The five categories that present most frequently are person (97.2%), wall (89.1%), floor (63.5%), ceiling (46.5%), and tree (42.3%). Each category can be found in at least 50 videos. Fig. 16 shows the detailed statistics of all the 150 categories.

A.4 Discussions of Data Characteristics

Animations. To enhance the diversity and generality of our VDW dataset, we include a small portion of animations (around 9% of frames), while the majority (91%) consists of real-world videos. The combination allows models to generalize well in natural scenes and produce robust predictions for animated videos. This could benefit various tasks that involve stylized videos, such as 3D video conversion, virtual reality, and video editing. Users can decide which parts to use, depending on their tasks and data requirements.

Disparity of Stereo Films. We mainly pursue data scale, diversity, and generality. Using other methods (*e.g.*, LiDAR, or Kinect) to annotate over 2 million frames in diverse scenes would incur much higher costs or may even be impractical. Thus, we adopt the disparity of stereo videos, which are more accessible and effective. However, the downside is that the disparity in stereo movies is not always trustworthy, as it could be adjusted for viewing comfort. We have implemented several measures to alleviate this problem, including removing overly unrealistic sequences and conducting rigorous data checking. Users can also combine the VDW with other datasets for training.

APPENDIX B
MORE IMPLEMENTATION DETAILS FOR NVDS+

B.1 Decoder Architecture

Here we specify the decoder architecture for video depth estimation. The decoder architecture is illustrated in Fig. 18. To fuse the depth-aware features from the backbone [48] and temporal features from the cross-attention module, feature fusion modules (FFM) [68], [69] and skip connections are adopted. Resolutions are gradually increased while channel numbers are decreased. At last, we use an adaptive output module to adjust the channel and restore the disparity maps.

As for the decoder of video semantic segmentation, we apply the simple and common architecture as prior arts [32], [44], [46], [48].

B.2 Feature Encoder

Feature Encoders [48], [67], [72], [95], [96] possess strong scene understanding and feature encoding capabilities, because of their comprehensive structural designs and model pre-training. Compared to the details in RGB images, feature encoders [48], [67], [72], [95], [96] extract high-level scene and semantic information with large receptive fields.



Figure 17: **More examples of our VDW dataset.** Sky regions and invalid pixels are masked out.

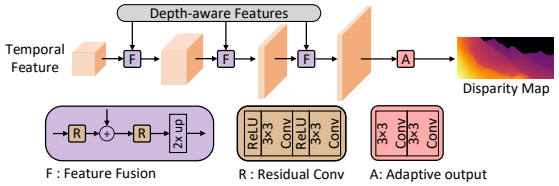


Figure 18: **The decoder architecture for depth estimation.**

Therefore, encoders with different structures, *e.g.*, convolutional [72], [95], [97] or attention-based [48], [67], [96] backbones, have been widely used in dense prediction tasks such as depth estimation and semantic segmentation. Our NVDS$^+$ also employs feature encoders [48], [72] to extract features.

To be specific, for video depth estimation, we adopt the Mit-b5 [48] in our NVDS$^+_{\textbf{Large}}$ model to encode depth-aware features, considering its strong performance and capacity. For the lightweight NVDS$^+_{\textbf{Small}}$ model, we utilize Mit-b0 [48] to achieve real-time processing. Besides, in our experiments of video semantic segmentation, we follow SSLTM [46] to leverage ResNet-50 [72] as the backbone, conducting fair comparisons with similar amounts of model parameters.

B.3 Loss Function

As mentioned in Sec. 3.2 in the main paper, the training loss for depth estimation consists of a spatial loss and a temporal loss. Here we specify the computation process.

For the spatial loss, we adopt the widely-used affinity invariant loss and gradient matching loss [7], [8] as $\mathcal{L}_s$. For the affinity invariant loss, let D and D^* denote the predicted disparity and ground truth respectively, we first calculate the scale and shift:

$$t(D) = median(D), s(D) = \frac{1}{M}\sum_{i=1}^{M}|D_i - t(D_i)|\,, \quad (12)$$

where M denotes the number of valid pixels. The prediction and the ground truth are aligned to zero translation and unit scale as follows:

$$\tilde{D} = \frac{D - t(D)}{s(D)}, \tilde{D}^* = \frac{D^* - t(D^*)}{s(D^*)}. \quad (13)$$

Then the affinity invariant loss can be formulated as:

$$\mathcal{L}_{af} = \frac{1}{M}\sum_{i=1}^{M}|\tilde{D} - \tilde{D}^*|. \quad (14)$$

Besides, we also adopt the multi-scale gradient matching loss [8], which can improve smoothness of homogeneous regions and sharpness of discontinuities in the disparity maps. The gradient matching loss is formulated as:

$$\mathcal{L}_{grad} = \frac{1}{M}\sum_{k=1}^{K}\sum_{i=1}^{M}(|\nabla_x R_i^k| + |\nabla_y R_i^k|), \quad (15)$$

where $R_i = \tilde{D}_i - \tilde{D}_i^*$, and R^k denotes the difference between the disparity maps at scale $k = 1, 2, 3, \cdots, K$ (the resolution is halved at each level). Following DPT [7], we set $K = 4$ and set the weight μ of $\mathcal{L}_{grad}$ to 0.5. The spatial loss can be expressed as:

$$\mathcal{L}_s = \mathcal{L}_{af} + \mu\mathcal{L}_{grad}, \quad (16)$$

As for the spatial loss of semantic segmentation, we adopt the widely-used cross-entropy loss for supervision.

Temporal Loss. In Sec. 3.2 of main paper, we mentioned that the temporal loss is masked with a visibility mask $O_{n\Rightarrow n-1}$ calculated from the warping discrepancy between frame F_n and the warped frame $\hat{F}_{n-1}$. This mask is obtained by:

$$O_{n\Rightarrow n-1} = \exp(-\gamma||F_n - \hat{F}_{n-1}||_2^2)\,. \quad (17)$$

We set $\gamma = 50$ and use bilinear sampling layer for warping.

B.4 Depth and Disparity

Here, we illustrate the reasons for using disparity in our implementations. Firstly, our VDW dataset is annotated with the disparity from optical flow [33], making it straightforward for us to work with disparity. Secondly, we utilize different versions of MiDaS and DPT [7], [8], [26] as the initial predictors, which produce relative disparity maps. Keeping the input and output settings of NVDS$^+$ similar to those of MiDaS and DPT [7], [8], [26], with disparity for training and inference, is convenient for the experiments. For other initial predictors that produce depth maps, their initial depth can be converted to disparity for input.

Besides, we also discuss the advantages and disadvantages of disparity and depth. Disparity is more sensitive to objects at close distances and can better distinguish between foreground objects and the background, which is beneficial for downstream tasks such as bokeh rendering [1], [2], 3D video conversion [3], and shallow depth of field effect [98]. On the other hand, depth maps can better differentiate distant objects, making them more suitable for autonomous driving tasks. Therefore, considering the applications in Sec. 5.7 of the main paper, using disparity could be more convenient for our experiments.

Appendix C
More Experimental Results

C.1 Depth Metrics

Here we specify the evaluation metrics for depth accuracy. we adopt commonly-applied depth evaluation metrics: Mean relative error (Rel) and accuracy with threshold t.

Mean relative error (Rel): $\frac{1}{M}\sum_{i=1}^{M}\frac{||D_i - D_i^*||_1}{D_i^*}$;

Accuracy with threshold t: Percentage of D_i such that $max(\frac{D_i}{D_i^*}, \frac{D_i^*}{D_i}) = \delta < t \in \left[1.25, 1.25^2, 1.25^3\right]$, where M denotes pixel numbers, D_i and D_i^* are prediction and ground truth of pixel i.

C.2 Robustness across Various Frame Rates

The Impacts of Frame Rates. Similar to image resolution in the spatial dimension, we consider frame rates as the temporal resolution of videos. Videos with high frame rates represent small sampling intervals between consecutive frames. The inter-frame motions of moving objects and the camera could be smooth and coherent, providing sufficient temporal information. Thus, it could be easier for video depth models to predict consistent depth results. In contrast, lower frame rates represent larger sampling intervals and reduced inter-frame continuity. With lower resolution and

Table 16: **Comparisons on VDW dataset.** The first 2 rows show the results of different single-image depth predictors. The next 5 rows contain video depth approaches. The last 2 rows consist of the results of our NVDS⁺. Best performance is in boldface. Second best is underlined.

Method	$\delta_1 \uparrow$	$\delta_2 \uparrow$	$\delta_3 \uparrow$	$Rel \downarrow$	$OPW \downarrow$
MiDaS-v2.1-Large [8]	0.651	0.857	0.935	0.288	0.676
DPT-Large [7]	<u>0.730</u>	<u>0.894</u>	<u>0.952</u>	<u>0.215</u>	0.470
ST-CLSTM [24]	0.477	0.709	0.838	0.521	0.448
FMNet [23]	0.472	0.716	0.837	0.514	0.402
DeepV2D [22]	0.546	0.722	0.835	0.528	0.427
WSVD [42]	0.637	0.831	0.914	0.314	0.462
Robust-CVD [19]	0.676	0.855	0.928	0.261	0.279
Ours-Large(MiDaS-v2.1-Large)	0.701	0.885	0.947	0.239	<u>0.148</u>
Ours-Large(DPT-Large)	**0.742**	**0.897**	**0.957**	**0.208**	**0.129**

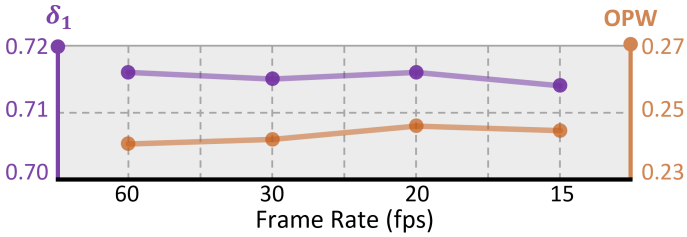


Figure 19: **Robustness across different frame rates.** The temporal window contains three reference frames. For a certain video, we conduct evaluations under frame rates from 15 to 60 fps. NVDS⁺ only exhibits minimal performance fluctuations, proving our robustness on various frame rates.

less information in the temporal dimension, it becomes more challenging to stabilize the flickers in the predictions.

Robustness on Different Frame Rates. As illustrated in Sec. A.3, the proposed VDW dataset includes source videos with diverse frame rates. Therefore, our NVDS⁺ can acquire strong robustness across various frame rates. As shown in Fig. 19, we conduct evaluations under varied frame rates from 15 to 60 fps for a certain video. The temporal window is fixed with three reference frames. Our model only exhibits minimal performance fluctuations. The results prove that our setting of the temporal window is appropriate and sufficient, showing robustness against the variations of fps.

We utilize a sequence of 60 fps from the VDW dataset for the experiment in Fig. 19. Directly sampling the original video will result in varied frames for evaluation, making the metrics incomparable. Instead, we reduce the frame rates by increasing the inter-frame intervals of reference frames. For example, for the target frame n, using reference frames $i \in \{n \pm 3, n \pm 2, n \pm 1\}$ represents the original frame rate of 60 fps, while adopting $i \in \{n \pm 6, n \pm 4, n \pm 2\}$ represents 30 fps. In this way, we can still obtain the predictions for all original frames and compare the performance.

The Ideal Setting of the Temporal Window. No single setting can be optimal for all the videos. Different scenes, frame rates, objects, and motions in videos could all have an impact. For example, we cannot guarantee that three reference frames work best for all the videos, such as some special videos with extremely high frame rates, *e.g.*, over 120 fps. But this could be simply solved by adjusting the input inter-frame intervals without the need to retrain the model.

Based on Table 11 (b) and Table 12 (b) in the main paper, we utilize three reference frames with the inter-frame interval $l = 1$ as the standard setting for all our experiments on different datasets [27], [35], [37], [40], [77]. Fig. 19 proves our strong robustness across various frame rates. Thus, users can simply follow the default setting for most videos. They can also adjust these settings, *e.g.*, the inter-frame interval, according to their specific videos and applications.

Table 17: **Comparisons on the Sintel dataset.** We only report CVD [18] and Zhang *et al.* [20] on the 12 videos with valid outputs, while other methods are on the 23 videos.

Method	$\delta_1 \uparrow$	$\delta_2 \uparrow$	$\delta_3 \uparrow$	$Rel \downarrow$	$OPW \downarrow$
MiDaS-v2.1-Large [8]	0.485	0.693	0.787	0.410	0.843
DPT-Large [7]	**0.597**	<u>0.768</u>	<u>0.846</u>	<u>0.339</u>	0.612
ST-CLSTM [24]	0.351	0.571	0.706	0.517	0.585
FMNet [23]	0.357	0.579	0.712	0.513	0.521
DeepV2D [22]	0.486	0.674	0.760	0.526	0.534
WSVD [42]	0.501	0.709	0.804	0.439	0.577
CVD [18]	0.518	0.741	0.832	0.406	0.497
Robust-CVD [19]	0.521	0.727	0.833	0.422	0.475
Zhang *et al.* [20]	0.522	0.727	0.831	0.342	0.481
Ours-Large(MiDaS-v2.1-Large)	0.532	0.731	0.833	0.372	<u>0.447</u>
Ours-Large(DPT-Large)	<u>0.591</u>	**0.770**	**0.849**	**0.335**	**0.403**

C.3 Flow-Guided Consistency Fusion

We provide a toy experiment to illustrate the principle of flow-guided consistency fusion, showing that the strategy does not introduce systematic errors in the presence of motion, which is presented in Fig. 20. From reference frame i to target frame n, we assume that a deep blue rectangle (as the foreground object) is moving horizontally, while the gray areas represent the static background (e.g., a wall), as shown in the first and second columns of Fig. 20. The bidirectional optical flow $FL_{n \Rightarrow i}$ and $FL_{i \Rightarrow n}$ can be calculated and visualized in the third and fourth columns. The white areas represent the static background where the optical flow is zero. The sky blue and the red areas showcase pixels with motion (*i.e.*, large flow magnitude), representing the moving object in frame n and frame i. For the relevance map W_i, we add the magnitude of $FL_{n \Rightarrow i}$ and $FL_{i \Rightarrow n}$ to perform the negative exponential transformation as Eq. 8 of the main paper. In this way, as shown in the last column of Fig. 20, values of the relevance map W_i are very low at the positions of the moving object in both frame n and frame i. This prevents the fusion of the reference frame i and preserves the depth D_n^{bi} of the target frame n, as Eq. 9 of the main paper. The result is correct because, for the moving rectangle, foreground and background pixels are misaligned, and the reference frames should not be fused.

Consequently, flow-guided consistency fusion does not introduce systematic errors in the presence of motion. For moving objects and regions, the depth of reference frames tends not to be fused due to misalignment. The original bidirectional depth D_n^{bi} of the target frame will be preserved.

To further prove the effectiveness, we showcase the detailed statistics of consistency improvements brought by flow-guided consistency fusion over the bidirectional inference with averaging. As shown in Fig. 21, the reduction rates of OPW are calculated for the 90 videos in the VDW test set. With MiDaS [8] or DPT [7] as the depth predictor,

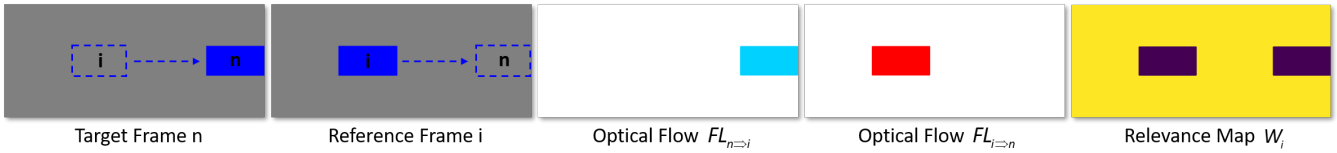
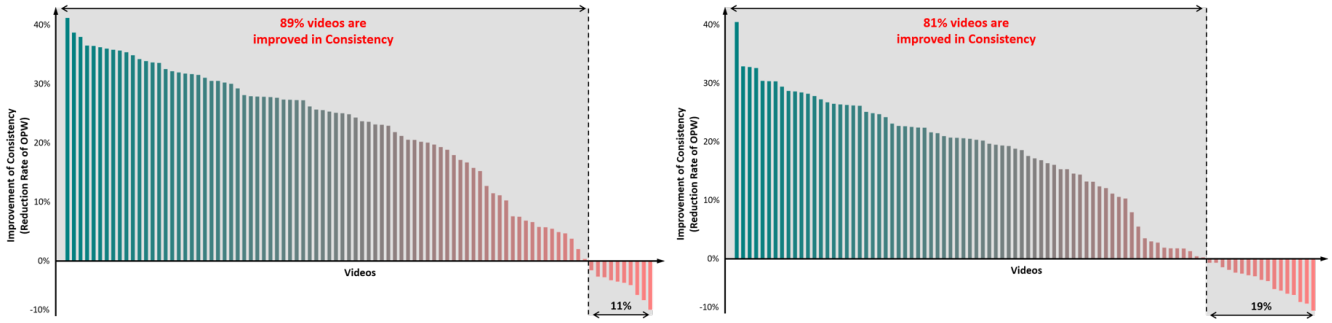


Figure 20: **The principle for flow-guided consistency fusion.** We conduct a toy experiment to illustrate the principle, proving that the flow-guided consistency fusion strategy does not introduce systematic errors in the presence of motion. For the relevance map W_i, brighter colors indicate higher values, while darker colors indicate lower fusion weights.



(a) MiDaS Initialization (b) DPT Initialization

Figure 21: **The effectiveness of flow-guided consistency fusion**. We showcase the detailed statistics of consistency improvements brought by flow-guided consistency fusion over the bidirectional inference with averaging. The reduction rates of OPW are calculated for the 90 videos in the VDW test set, using MiDaS [8] or DPT [7] as varied depth predictors.

89% and 81% of all the videos achieve better consistency (above the X-axis) respectively. The depth accuracy is also maintained as proved by Table 5 of the main paper. Overall, bidirectional inference and flow-guided consistency fusion are simple but effective methods for improving consistency without introducing systematic errors, because of the adaptive fusion based on bidirectional optical flow, motion amplitude, and relevance maps. The experiments demonstrate that our approach only requires optical flow and works well for most testing videos.

On the other hand, the relations among camera motion, object motion, and depth variations could be complex in different scenarios. Our assumptions and methods could not fully cover all corner cases due to the diversity of real-world videos. We also try to explore some mechanisms that could be more comprehensive theoretically. However, these techniques introduce new problems in practice. For instance, camera motion compensation [99] can be adopted to decouple the camera and object motion. But their reliance on camera parameters (*e.g.*, the FOV) is impractical for in-the-wild videos, leading to failure cases and artifacts. Therefore, we use bidirectional optical flow to perform motion compensation in the flow-guided consistency fusion.

C.4 Zero-shot Evaluations and Model Finetuning

As presented in Table 18, we report the results of NVDS$^+_{\textbf{Large}}$ with zero-shot evaluations (*i.e.*, only trained on the VDW dataset) and model finetuning on the NYUDV2 [37] dataset. For zero-shot evaluations, our model improves both the temporal consistency and depth accuracy over the depth predictors [7], [8], showing the generalization ability of our method. Besides, the finetuning can further improve the depth accuracy for closed-domain applications, *e.g.*, the static indoor scenes of the NYUDV2 [37] dataset.

Table 18: **Zero-shot evaluations and model finetuning.** DPT-Large [7] and MiDaS-v2.1-Large [8] are adopted as different depth predictors. We report the results of NVDS$^+_{\textbf{Large}}$ with zero-shot evaluations (*i.e.*, only trained on the VDW dataset) and model finetuning on the NYUDV2 [37] dataset.

Method	$\delta_1 \uparrow$	$OPW \downarrow$
DPT [7]	0.928	0.811
Zero-Shot(DPT)	0.930	0.351
Finetune(DPT)	**0.950**	**0.339**

(a) DPT Initialization

Method	$\delta_1 \uparrow$	$OPW \downarrow$
MiDaS [8]	0.910	0.862
Zero-Shot(MiDaS)	0.919	**0.332**
Finetune(MiDaS)	**0.941**	0.347

(b) MiDaS Initialization

C.5 Runtime Analysis

For the NVDS$^+_{\textbf{Small}}$ model, we report the runtime of each component in milliseconds (ms), including the depth predictors [8], [26], the feature encoder, the cross-attention module, and the decoder. The stabilization network achieves faster inference speed than lightweight depth predictors [8], [26]. Combining all components, NVDS$^+_{\textbf{Small}}$ can still achieve real-time processing of over 30 fps.

C.6 More Quantitative Comparisons

In the main paper, only δ_1, Rel, and OPW are reported. The additional results on the VDW and the Sintel [40] dataset are shown in Table 16 and Table 17. Besides, as CVD [18] and Zhang *et al.* [20] cannot produce results on 11 of 23 videos in Sintel [40] dataset, we additionally report the results on the other 12 videos in Table 20.

C.7 More Qualitative Results.

We show more visual comparisons in Fig. 22 and 23. We draw the scanline slice over time. Fewer zigzagging pattern means better consistency. Please refer to our demo video and project page for more video results and comparisons.

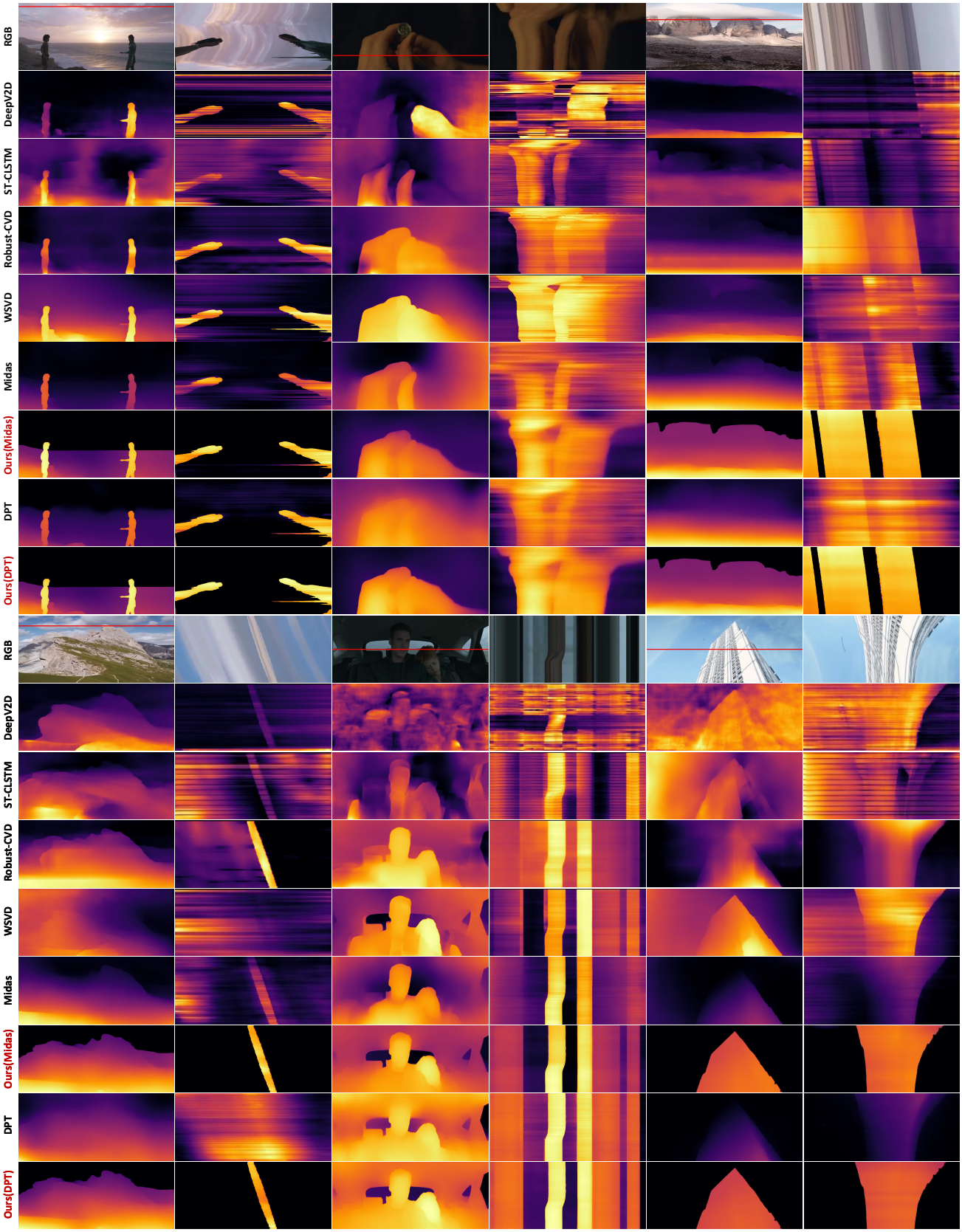


Figure 22: **More qualitative results on natural scenes.** The first image in each pair is the RGB frame, while the second is the scanline slice over time. Fewer zigzagging pattern means better consistency.

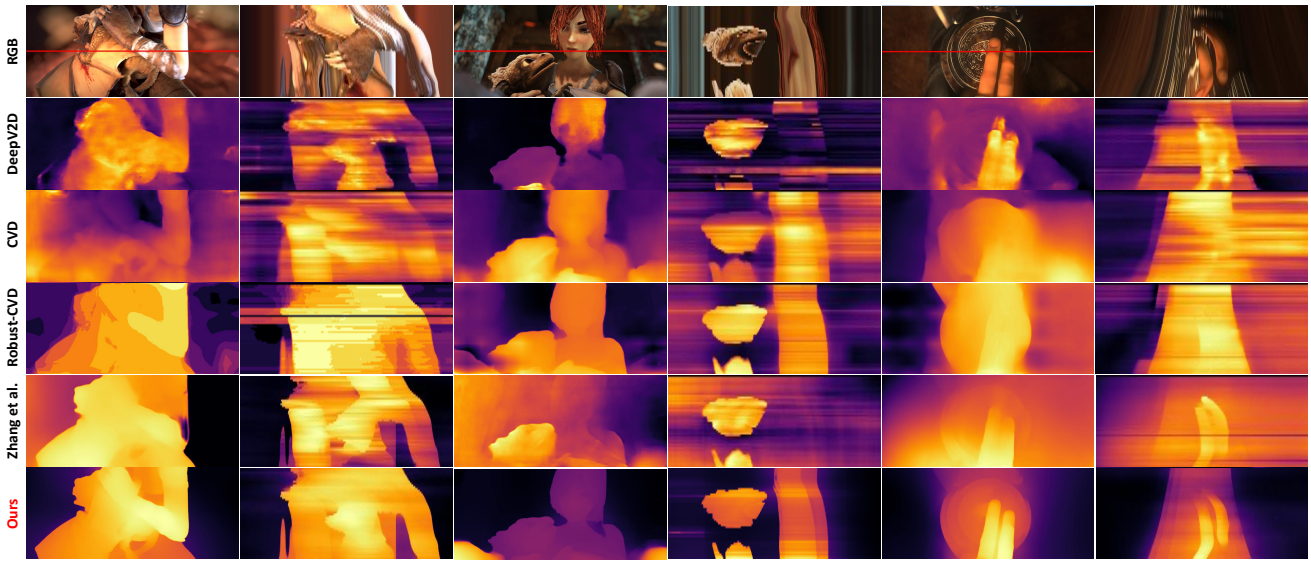


Figure 23: **Qualitative results on Sintel [40] dataset.** We compare the results of DeepV2D [22], CVD [18], Robust-CVD [19], and Zhang *et al.* [20]. Without relying on test-time training [18], [19], [20], we conduct zero-shot evaluations on Sintel [40] and achieve significantly better performance than those test-time-training-based methods [18], [19], [20].

Table 19: **Runtime of the lightweight NVDS$^{+}_{\text{Small}}$ model.** We report the runtime of each component to predict one 896 × 384 frame on an NVIDIA RTX A6000 GPU. The NVDS$^{+}_{\text{Small}}$ model shows high efficiency for real-time applications.

Module	Component	Runtime (ms)	Overall (ms)
Depth Predictor	DPT-Swin2-Tiny [26]	24.18	24.18
	MiDaS-v2.1-Small [8]	22.35	22.35
Stabilization Network	Feature Encoder	1.34	6.29
	Cross-attention	0.89	
	Decoder	4.06	

Table 20: **Comparisons on the 12 videos of Sintel [40] dataset.** We test the 12 videos that CVD [18] and Zhang *et al.* [20] can produce results for comparisons.

Method	$\delta_1 \uparrow$	$\delta_2 \uparrow$	$\delta_3 \uparrow$	$Rel \downarrow$	$OPW \downarrow$
MiDaS-v2.1-Large [8]	0.670	0.853	0.902	0.246	0.712
DPT-Large [7]	**0.747**	0.874	0.917	**0.196**	0.671
ST-CLSTM [24]	0.477	0.711	0.827	0.366	0.547
FMNet [23]	0.492	0.728	0.825	0.363	0.516
DeepV2D [22]	0.509	0.735	0.827	0.384	0.575
CVD [18]	0.518	0.741	0.832	0.406	0.497
Zhang *et al.* [20]	0.522	0.727	0.831	0.342	0.481
WSVD [42]	0.621	0.822	0.891	0.305	0.581
Robust-CVD [19]	0.673	0.848	0.888	0.284	0.447
Ours-Large(MiDaS-v2.1-Large)	0.701	0.867	0.918	0.215	0.403
Ours-Large(DPT-Large)	0.741	**0.878**	**0.925**	0.201	**0.392**

APPENDIX D
IMAGE ATTRIBUTION

We properly attribute the sources of all images and figures throughout our main manuscript and supplementary document, as presented in Table 21. We also specify the images from movies, documentaries, and animations with their IMDB movie numbers. Web videos and public datasets do not have IMDB numbers, with – as representation.

Table 21: **Attribution of the images in our main manuscript and supplement.** We report the image attribution of all figures throughout our paper.

Figures	Types	Attribution	IMDB Numbers
		Main Manuscript	
Fig. 1	Movie	Everest	2719848
Fig. 2	Movie	Everest	2719848
Fig. 4	Animation	Frozen 2	4520988
	Movie	Eternals	9032400
Fig. 5	Web Video	YouTube	–
	Documentary	Jerusalem	2385006
	Documentary	Kingdom of Plants	2117380
	Animation	Kung Fu Panda 3	2267968
	Movie	The Hobbit 2	1170358
	Movie	The Great Gatsby	1343092
Fig. 7	Movie	Eternals	9032400
	Animation	Frozen 2	4520988
Fig. 8	Public Dataset	DAVIS [77]	–
Fig. 9	Movie	Eternals	9032400
Fig. 10	Public Dataset	CityScapes [50]	–
Fig. 11	Public Dataset	NYUDV2 [37]	–
Fig. 12	Movie	Eternals	9032400
	Movie	Everest	2719848
	Web Video	NSFF [6] Demo	–
Fig. 13	Movie	Eternals	9032400
	Movie	Fantastic Beasts and Where to Find Them	3183660
Fig. 14	Public Dataset	Sintel [40]	–
		Supplementary Document	
Fig. 17	Web Video	YouTube	–
	Web Video	bilibili	–
	Documentary	Jerusalem	2385006
	Documentary	Kingdom of Plants	2117380
	Documentary	Little Monsters	11019830
	Documentary	Deepsea Challenge	2332883
	Animation	Kung Fu Panda 3	2267968
	Animation	Coco	2380307
	Movie	The Great Gatsby	1343092
	Movie	Mission: Impossible-Fallout	4912910
	Movie	Doctor Strange	1211837
	Movie	Transformers: Age of Extinction	2109248
	Movie	The Legend of Tarzan	0918940
	Movie	Exodus: Gods and Kings	1528100
Fig. 22	Web Video	YouTube	–
	Web Video	bilibili	–
	Movie	Eternals	9032400
	Movie	Fantastic Beasts and Where to Find Them	3183660
Fig. 23	Public Dataset	Sintel [40]	–